Development of a Geometric Modeling Strategy for the Generation of Representative Unit Cells in 2D Braids

José Rothkegel[a], Benjamin Renson[a], Michaël Bruyneel[a,b], Ludovic Noels[a,*]

[a]*Department of Aerospace and Mechanical Engineering Computational "& Multiscale Mechanics of Materials (CM3) University of Liege"" 9 Allee de la Decouverte 4000 Liege Belgium*
[b]*GDTech S.A. 7 Avenue de l'Expansion 4432 Ans Belgium*

Abstract

This article presents, tests and validates a method for generating representative unit cells of braided composites based on a geometrical approach. The method focuses on the geometry of the tows and uses surface minimization to obtain the minimal equivalent area of a central surface that is used for the generation of volumes and orthotropic mechanical properties of the tows. The homogenization of the yarns is solved using analytical equations and the homogenization of the cell is solved using a representative volume element technique. The robustness of the method is evaluated using a benchmark comparison with experimental and numerical results to validate the generated ge.ometry. The method is also tested and shown to be robust in modeling the geometry for several values of geometrical parameters of the tows without user intervention, including for configurations yielding a high cover factor.

Preprint submitted to Composite Structures (C) 2024; Licensed under the Creative Commons (CC-BY-NC-ND); formal publication on: 10.1016/j.compstruct.2024.118503

Keywords: Braiding, Bezier surface, Lagrange multiplier, Dirichlet energy

1. Introduction

Textile composite materials are a broad spectrum of material types that are built by a distribution of fiber materials into a resin matrix. The applications of textile composites range from industrial to domestic applications. Its influence on the industrial domain has increased in the past decades, into sectors such as the aerospace, automotive and marine industries [1].

The present work is focused on braided composites, which are one type of composite material that can be distinguished by their interlaced structure [2]. 2D and 3D braided composites are manufactured in two steps: preforms are first produced and then impregnated with a binding material (*i.e.* the matrix).

*Corresponding author, Phone: +32 4 366 48 26, Fax: +32 4 366 95 05
Email addresses: ji.rothkegel@uliege.be (José Rothkegel), michael.bruyneel@gdtech.eu (Michaël Bruyneel), l.noels@ulg.ac.be (Ludovic Noels)

Braided preforms are produced with a braiding machine composed of a central mandrel and a breading head with a large number of fiber carriers. Depending on the order on how the yarns are laid on the preform, different patterns are obtained, where each pattern has some geometrical conditions to satisfy in order to be reproduced, linking all the geometrical parameters together. Typical 2D patterns are diamond, regular and hercules, as shown in Fig. 1.

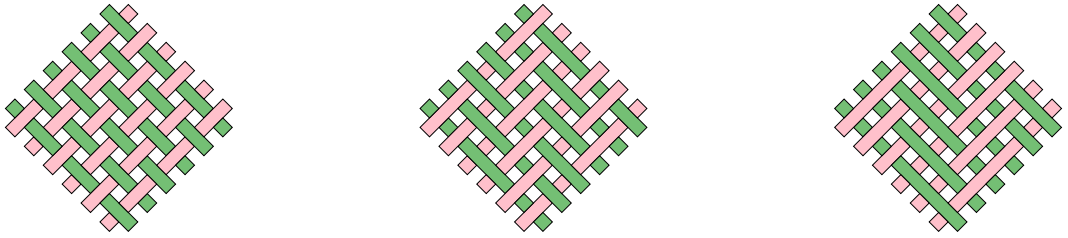

(a) Diamond (b) Regular (c) Hercules

Figure 1: Typical 2D bi-axial patterns

As the use of textile composites increases, numerical methods have been developed in order to predict their mechanical responses. However, detailed methods, such as the Finite Element (FE) models, require an accurate geometrical description of the composites, and in particular of the fibers distribution, organization and orientation in the matrix, in order to provide reliable results. The tows representing the fiber yarns embedded in the matrix can be modeled as an orthotropic material, but this requires the fibers directions to be obtained from a micro-structure description. The modeling of the fibers is usually achieved using simple modified sinusoidal functions but proves to become increasingly challenging as the undulation path can be highly distorted for the more compact configurations. There is thus a need to develop micro-structure generation tools, from which the tows direction can be extracted, that can be used to feed the mechanical analyzes.

1.1. State of the Art

In broad terms, the modeling strategies of braided composites can be classified into two main categories: analytical methods and numerical methods.

1.1.1. Analytical Methods

Analytical methods present the first attempt for obtaining usable models to obtain the mechanical properties of braided composites. The most common models are the Classical Laminate Plate Theory-based models (CLPT) and Volume Averaging Models(VAM).

One of the first proponents of the method of the determination of the stiffness and strength of woven fabric composites using a CLPT-based approach was proposed by Ishikawa and Chou [3, 4, 5, 6]. Further work based on their approach has been developed, such as the work of Yang et al. [7], which expands on

the work of Ishikawa and Chou, obtaining a more general model, not restricted to a particular weaving or braiding technique. Naik and Shembekar [8, 9, 10], extended Ishikawa and Chou's 1D fiber inclination model into a simple but accurate two-dimensional version, taking into account fiber continuity and undulations in the fill and warp directions. Redman and Douglas [11] innovated by developing a simple "CLPT/rule-of-mixtures" based model for tri-axial braided composites. Raju and Wang [12] developed a more accurate geometry to characterize undulating fibers in the fill and warp directions, starting from Ishikawa and Chou's model [3]. Naik and Ganesh [13] expanded the existing methods to take into account the yarn geometry and cross-section, including this way the fiber volume fraction. Aggarwal et al. [14] presented a generalized CLPT-based model to predict the in-plane elastic constants of two-dimensional diamond braided composites.

CLPT-based models are limited due to the underlying assumptions of the laminate theory: it assumes that the laminate is sufficiently thin, which may not be valid for braided composites due to the thickness and the undulations of the braid yarns. It also considers a plane stress state. These models are thus very limited for the analysis of complex, more realistic structures.

A first VAM was applied by Kregers and Melbardis [15], Kreger and Teters [16, 17] to determine the properties of spatially reinforced composites. Byun [18] developed a detailed model for the prediction of the geometric characteristics, crimp yarn angle, fiber-volume fraction, and three-dimensional engineering constants of 2D braided textile composites. Quek et al. [19] proposed a model for the calculation of the effective linear elastic stiffness of a 2D tri-axial flat braided composite material. Shokrieh and Mazloomi [20] created a new model in which the braided composite is considered as consisting of three layers Quek et al. [19]. El-Hajjar et al. [21] used and compared three different models to predict the elastic behavior of quasi-isotropic tri-axial braided composites. They all show a reasonable prediction of the elastic properties within the range of the properties measured. Similarly, Kier et al. [22] also developed a model whose estimations were comparable with experimental and FE results.

More recently, Heide-Jørgensen et al. [23] have developed an analytical, three-dimensional, multiscale homogenization for plain-woven hybrid composites, using sinusoidal expressions to describe the geometry. Their approach can consider the debonding of the fiber from the matrix material at the microlevel.

1.1.2. Finite Element Methods

FE models for textile composites typically use a multi-scale modeling procedure. In general, to obtain the mechanical properties of an immediate larger scale (*e.g.* micro to meso and meso to macro), a homogenization technique is used. In textile composites it is possible to apply this type of techniques since a repeating pattern can be identified. By definition, a Representative Unit Cell (RUC) is the smallest repeating part of a material that is assumed perfectly periodic and regular.

Textile composites typically have three structural levels: the micro, meso, and macroscopic levels. The meso-level is the key step in the multilevel calculations for textile composites as it makes the link between

the micro and macro-level analysis.

Microscopic level: corresponds to the scale of the basic constituents, *i.e.* fibers and matrix, within the braid yarns. This step is commonly performed using analytical micro-mechanics equations, such as the models presented by Halpin [24] and Chamis [25].

The Mesoscopic level: corresponds to the scale of the braid yarns. Meso-scale modeling allows for the prediction of braided composite material mechanical properties starting from mechanical properties of the tows (computed during the micro-scale modeling) and the matrix.

The Macroscopic level: corresponds to the overall structure scale. Macro-scale modeling allows to predict the elastic behavior of an entire braided composite structure under external global loading conditions.

2D FE models focus on one of the most reputed methodology called the Braiding Through-the-Thickness (BTT) method. The BTT method, also known as Braiding through-the-Thickness Integration Points (BTIP), is a semi-analytical model. Xiao et al. [26] created the Pure Matrix Model. The authors used the same layered shell approach as their predecessors but modeled matrix pockets by adding layers of pure matrix within the sub-cells. Following Cater et al. [27], Cater et al. [28] utilized the Pure Matrix Model (PMM) and Absorbed Matrix Model (AMM) to approximate the behavior of single-ply and multi-ply braid coupons subjected to tensile tests. Starting from the work of Sorini et al. [29], Cater et al. [30] used the AMM combined with a top-down approach to predict both the strengths and failure modes of braided composites. More recently, García-Carpintero et al. [31] proposed an efficient numerical methodology based on a multi-material shell (MMS) model for the analysis of the mechanical behavior of tri-axial braided composites subjected to tensile loads.

Since braided composites consist of a 3D complex interlacing of tows, both the geometrical model and the mechanical analysis ought to be three dimensional in order to capture the interlacing effect. A detailed road map for the examination of textile and braided composites using a 3D FE approach was proposed by Lomov et al. [32]. Goyal et al.[33, 34] focused on the analysis of 2×2 regular braids using a 3D FE analysis. They use typical FE models, accompanied with boundary conditions supposed to reflect the periodicity of the mesostructure. An important result of the analysis is that braided materials are essentially orthotropic. Quek et al. [35] analyzed and modeled the RUC of carbon 2D tri-axial braided composite in order to predict its effective elastic stiffness and strength using the FE method. Li et al. [36, 37] proposed a meso-scale FE model for examining the behavior of tri-axial braided polymer matrix composites. Later, Li et al. [38] used this model for failure study on straight-sided braided composite specimens. In 2012, Xu et al. [39] presented a general modeling method of braided structures and predicted the material properties of bi-axial and tri-axial braided textile composites. A micro-mechanical approach was adopted to compute the material properties of the tows. Similarly, Mian et al. [40] developed a 3D FE meso-scale model with PBC

to predict braids materials properties. Mbacke [41] also studied the variation of mechanical properties with the braiding angle using a multi-scale approach with two homogenization stages (one at the microscopic level and one at the mesoscopic level).

More recently, Wehrkamp-Richter et al. [42] proposed a novel simulation framework for accurately predicting the mechanical response of highly compacted tri-axial braided composites. A workflow to generate unit cells with a realistic internal geometry was presented. Local inter-penetrations were removed via a fictitious thermal simulation step, and then a compaction simulation was performed to get the target fiber volume fraction. The framework was validated by a detailed comparison with experimental results. Furthermore, Wehrkamp-Richter et al. [43] applied their simulation framework to predict the non-linear mechanical response of tri-axial braided composites under multiple loading conditions.

The work of Goda and Ganghoffer [44] presents a homogeneous, anisotropic strain-gradient continuum model aiming at substituting 3D heterogeneous porous or composite materials, such as woven materials. The effective properties are obtained based on the response of the representative volume element or unit cell of the initial structure under prescribed boundary conditions. Mixed boundary conditions comprising both traction and displacement boundary conditions are applied on the structure boundaries to identify the equivalent 3D strain-gradient elasticitymodel.

1.1.3. Geometric Description of the RUC for Mesoscopic Modeling

For braided composites, the generated finite element model used to perform the modeling of the RUC requires the construction of a geometrical model that describes the undulation paths of the different tows present. The undulation path is dependent on the pattern, *i.e.* diamond, regular or hercules.

However, a braided composite material composed of multiple layers can exhibit small undulations within the axial tows path. This is due to the compaction and shifting of the bias yarns in the axial direction during the manufacturing process. These undulations were observed, among others, by Zhang et al. [45]. However, they concluded that this undulation effect does not appear to influence the effective elastic properties significantly, hence axial tows are usually modeled as following a straight path. The bias tows are modeled in two main ways:

Sinusoidal function: this is the simplest way to model the undulating path of the tows. It has been used broadly, like in the works of Zhang et al. [46] and Wehrkamp-Richter et al. [42]. The pure sinusoidal function is easy to implement but is limited to the diamond braiding pattern only.

Circle arc function: this is an alternative way to model braid yarns undulation. The undulation path can be approximated with arcs. It is usable with diamond braiding pattern only.

Inter-penetrations occur when the volume of two or more tows penetrate each other. To avoid inter-penetrations, several solutions have been proposed, as summarized by García-Carpintero et al. [47]:

- Lomov et al. [32] proposed to separate the interpenetrating volumes and to compact them back via a solution of an intermediate FE problem.
- Stig and Hallström [48] did the same, but by inflating yarn volumes which are artificially thinned.
- Crookston et al. [49] simply added clearance between the yarns, but this solution gives an erroneous fiber volume fraction to the model.
- García-Carpintero et al. [47] proposed a methodology based on a virtual thermal expansion and compression. There also exist solutions that treat the interpenetration problem by modifying the cross-sectional shape of the bias tows directly in the CAD model [33, 42].
- Wintiba et al. [50] developed a methodology that considers a geometrical approach, in which the contact between the yarns is resolved directly with the introduction of an implicit tension.
- Li et al. [51] introduced a level-set approach to eliminate the interpenetration of the yarns.

1.1.4. Present Work Contribution

The present work introduces a novel strategy to generate the RUC based on geometric relations and an equivalent minimization of the length of the fiber tows.

Contrarily to geometrically-based methodologies developed to generate the RUC which requires an *a priori* knowledge of the shape of the tows in order to avoid their interpenetration, and can thus be limited in terms of the combination of the imposed shape and braiding parameters, the present geometrical approach uses a decomposition of the geometry of the tows into a cross section and a central surface and applies a minimization technique to compute the minimal equivalent surface area of the central surface. This approach thus replaces the usual assumption of sinusoidal and straight paths for the tows by a Bézier surface approach, which adds flexibility to the tow shapes that can be obtained while avoiding interpenetration. This, *in fine* allows obtaining the geometry of the tows without making any *a priori* assumption of the shape of the undulation path, and eventually allows for an automatic generation of the geometry.

This approach allows for a calculation of the shape of the tows considering the interaction of opposing bias tows single-handily. Some simplifications can be made to include the repetitivity of the shape of the tows in the RUC which improve the performance of the method. The approach reduces the computational costs and is robust in generation for a wide range of geometrical parameters. The cover factor that can be obtained is close to 1.

When performing homogenization, the proposed model considers orthotropy in the tows, as the result of the fibers embedded in the resin matrix. The fibers directions that are used in the calculation of the orthotropic mechanical properties of the tows are directly obtained from the central surface used to generate the geometry.

The present article is divided into the following sections: introduction, method, results and conclusions. The method Section 2 consists of a description of pertinent concepts used by the generation algorithm and its implementation, where starting from a flowchart describing the full method, each individual subsection is developed. The results reporyed in Section 3 verify and validate the generation method through a chosen benchmarks and pertinent comparisons with both numerical and experimental literature results. The robustness of the generator is then ascertained by varying the geometrical parameters and it is shown that the approach allows generating a wide range of RUC including ones with high cover factors close to 1. Finally the computational costs associated to the RUC generation, and the homogenized properties estimation are reported and discussed.

2. Proposed Method

2.1. Definitions

The definitions presented in this subsection are intended for a clearer explanation of the method and serve as the basis for its development.

2.1.1. Cross-Section

The cross sections of the tows are defined as fixed and are obtained using power ellipses. The benefit of using power ellipses lies in the fact that a single parameter can change the shape of the cross section between lenticular and elliptic, as initially presented in Crookston [52]. The formula used here is a sinusoidal formula presented in Wehrkamp-Richter et al. [42]

$$y = \pm \frac{t}{2} \cos\left(\frac{x\pi}{w}\right)^n , \tag{1}$$

where t is the thickness and w is the width of the cross section, as shown in Fig. 2a. For different values of n we get different shapes, as shown in Fig. 2b.

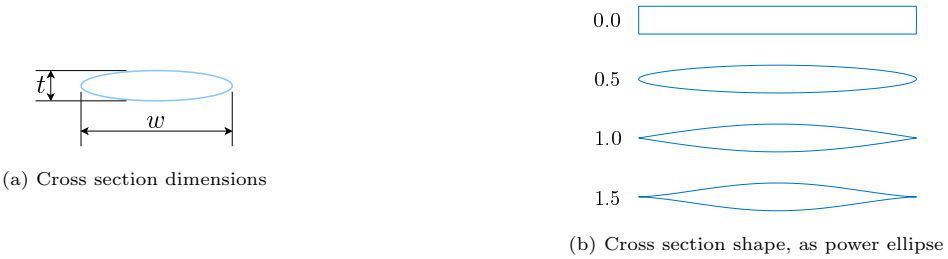

(a) Cross section dimensions

(b) Cross section shape, as power ellipse

Figure 2: Cross section dimension and shape for different values of n

2.1.2. Pattern

The patterns used in the present work are tri-axial patterns, which are based upon bi-axial patterns, such as shown in Fig. 1, adding yarns along the axial direction, *i.e.* the direction of advance of the braiding machine. The two tri-axial patterns that are considered in this article are diamond and regular, as shown in Fig. 3.

(a) Diamond

(b) Regular

Figure 3: Typical 2D tri-axial patterns

2.1.3. Representative Unit Cell (RUC)

As mentioned before, a RUC is the smallest repeating part of a material that is assumed perfectly periodic and regular. It depends on each pattern. For the present work, the RUC for the diamond pattern can be seen in Fig. 4a and the RUC for the regular pattern can be seen in Fig. 4b.

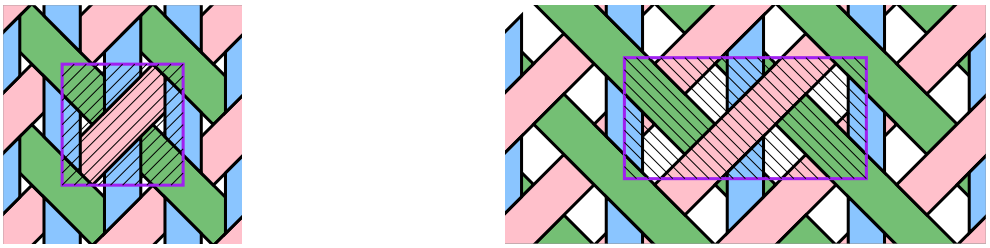

(a) RUC of the diamond pattern

(b) RUC of the regular pattern

2.1.4. Cover Factor

The calculation of the cover factor is evaluated using a polygonal approach, where the different surface areas can be obtained using Boolean operations. The procedure can be summarized as:

1. A rectangle is drawn, to represent the unit cell and the rectangles that represent the different tows, as shown in Fig. 5a.
2. Using Boolean operations the areas of the cell between the tows can be obtained. A detail of these areas is shown in 5b, in green.

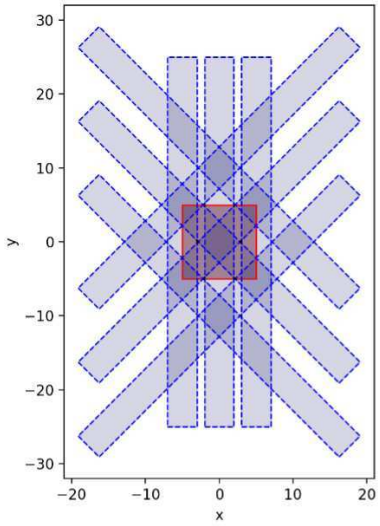

(a) General distribution of the tows in the cell

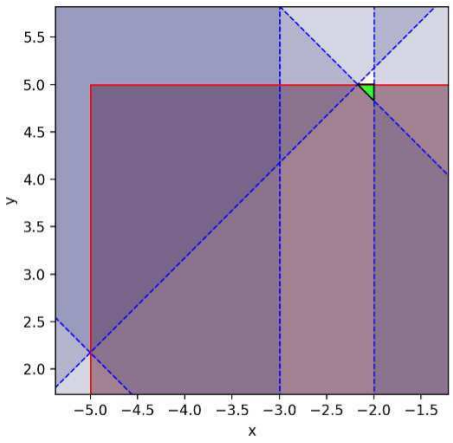

(b) Detail of the top left corner of the cell

Figure 5: Polygon model for the calculation of cover factor

The implementation has been done in Python, using the Shapely library. The cover factor is finally calculated as

$$C_f = \frac{A_{RUC} - \sum A_{space}}{A_{RUC}} \,. \tag{2}$$

where A_{RUC} corresponds to the projected surface area of the cell, shown in red in Fig. 5a, and A_{space} corresponds to the projected surface area of the space between tows, shown in green in Fig. 5b.

2.1.5. Volume Fraction

The total volume fraction of the RUC represents the ratio between the volume of the fibers and the total volume of the RUC. It depends on the fiber volume fraction of each tow and the tow volume fraction in the RUC.

The fiber volume fraction is the ratio between the volume of fibers in the tow and the total volume of the tow.

$$V_{f,t} = \frac{v_{f,t}}{v_t} \,, \tag{3}$$

where $v_{f,t}$ is the volume of the fibers and v_t is the volume of the tow. Subscript "t" stands for either axial or bias tow.

The fiber volume fraction of the representative unit cell is hence obtained as

$$\begin{aligned} V_{f,RUC} &= \frac{V_{f,a} \cdot v_a + V_{f,b} \cdot v_b}{v_{RUC}} \\ &= V_{f,a} \cdot V_a + V_{f,b} \cdot V_b \,, \end{aligned} \tag{4}$$

where subscripts "a" and "b" respectively stand for axial and bias tows.

The axial and bias tow volume fractions in the unit cell, V_a and V_b, are determined by the architecture and arrangement of tows in the RUC. The fiber volume fraction in the axial and bias tows, $V_{f,a}$ and $V_{f,b}$, depends mainly on the compaction of the fibers and the space available for the matrix resin. In general, the fiber volume fraction in the tows is around $80 - 85\%$, with an theoretical upper limit of approximately 90.69%. This upper limit is calculated assuming a compaction in hexagonal form, as shown in Fig. 6, and calculated as

$$A_{circ} = \pi \cdot r^2 \,, \tag{5}$$

$$A_{hex} = \frac{6}{\sqrt{3}} r^2 \,, \text{ and} \tag{6}$$

$$V_f = \frac{A_{circ}}{A_{hex}} = \frac{\pi\sqrt{3}}{6} \approx 0.9069 \,. \tag{7}$$

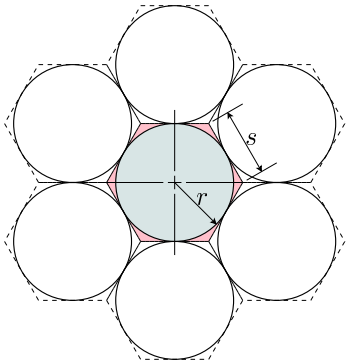

Figure 6: Hexagonal distribution of fibers in tow

It is common to describe a tow according to the number of fiber filaments n (in thousands or k) present in its micro-structure and the diameter of a single tubular fiber filament d (in μm). Using these two parameters, the area A_f occupied by the fiber filaments within a tow cross-section can be computed.

$$A_{f,t} = \frac{\pi d^2}{4} n \tag{8}$$

Knowing the area of the tows cross-section, the Fiber Volume Fraction within a tow can be calculated, with L_t defining the length of the tow as

$$V_{f,t} = \frac{v_{f,t}}{v_t} = \frac{A_{f,t} \cdot L_t}{A_t \cdot L_t} = \frac{A_{f,t}}{A_t} \,. \tag{9}$$

2.1.6. Distribution and Directions

The distribution of the tows in the $x-y$ plane determines the type of braiding pattern and is fundamental in the characterization of the properties of the composite. The axial tows are distributed along the x direction

and are aligned with the y direction, with a separation s_{axial} that is measured between the central axis of each axial tow, as shown Fig. 7.

The bias tows are rotated by an angle θ with respect to the axial tow and are distributed with a distance s_{bias} along the y direction, as shown in Fig. 7.

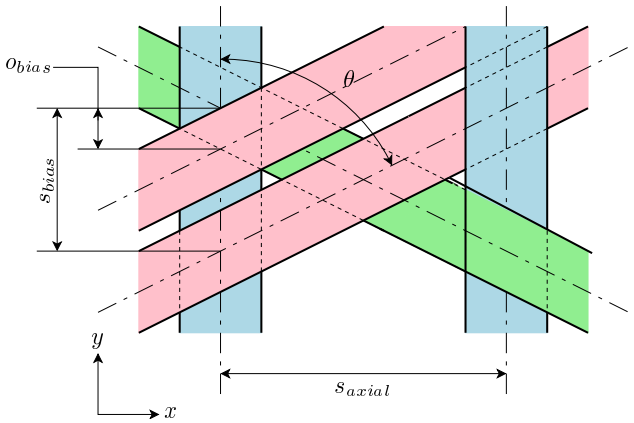

Figure 7: Distribution and dimensions in the $x - y$ plane.

2.1.7. Central Surface

The method considers initially the decomposition of the geometry of each tow into a central surface and its original cross section, as shown in Fig. 8. This type of decomposition allows for a modification of the central surface whilst keeping the original cross section unperturbed.

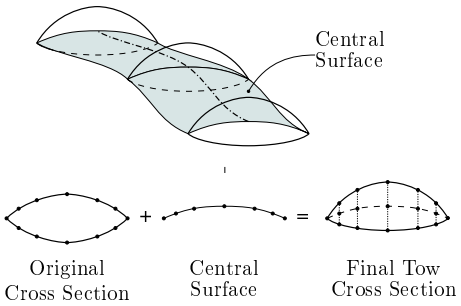

Figure 8: Central surface definition.

The central surface of each tow is modeled using Bézier patches, which allows to modify the surface by means of the control points of the surface.

Bézier surfaces constitute a flexible description of parametric surfaces. The basic idea behind using a Bézier surface is to minimize the length of said surface in a certain direction, as it will be later detailed. A main advantage of considering Bézier surfaces is that there exist explicit, analytical expressions that can be used to evaluate the surface sensibility with respect to the position of the control points, expressions

that can be in turn used to minimize the surface area. It is worth noting that the proposed method can be applied to other type of surfaces, such as NURBS via the Bézier extraction. However, although Bézier surfaces are able to describe the central surface of the tows, some numerical problems might arise when calculating the sensitivities if the control points are too close from each other.

The central surface serves as a base for the calculation of the orthotropic properties of the tows. The direction of the fiber at a point is considered to follow the direction of the surface when the point is projected in the z direction. Considering that the central surface is built using a Bezier surface, the direction of the fiber is obtained by deriving the surface in the given direction and normalizing. As it can be seen in Fig. 9, considering that the direction of the fiber coincides with the local direction v, the process is:

1. projecting point P in global coordinates (x, y, z) onto the local coordinates of the surface (u, v);
2. calculating the surface derivative t in direction v as

$$t = \frac{\partial S}{\partial v}\,; \tag{10}$$

3. finally, normalizing and obtaining the direction as

$$\hat{t} = \frac{t}{|t|}\,. \tag{11}$$

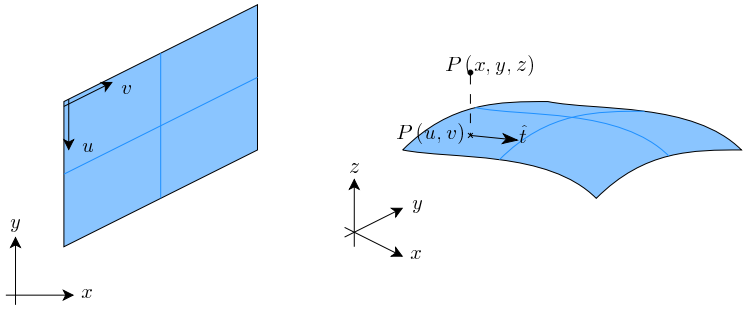

Figure 9: Surface direction used for orthotropy modeling.

2.2. Micro-structure generation

2.2.1. Overview of the Method

A general form of the proposed method is presented in Fig. 10 and is subsequently detailed.

The method starts with a guess initial geometry, where the distribution of the tows is determined. Once it is done, the surface area of the central surface is minimized, avoiding interpenetration of the tow volumes. This configuration allows for the sensitivity to be calculated in such a way that the adjacent surfaces are tangent. The configuration is updated using the obtained sensitivity.

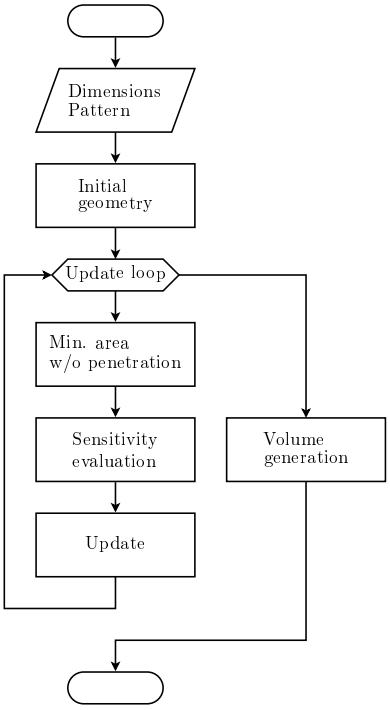

Figure 10: General view of the method.

2.2.2. Initial Geometry

The initial geometry begins with the initial distribution of the different tows in the $x-y$ plane, as follows:

1. Distribute the axial tows in the x direction, considering s_{axial}. The axial tows are considered fixed and are not modified.
2. Lay the bias tows considering the axial separation s_{axial}, the braiding angle θ and the type of braiding pattern, imposed by the offset of the bias tows o_{bias} in the y direction. For simplicity, we will consider only two bias tows.

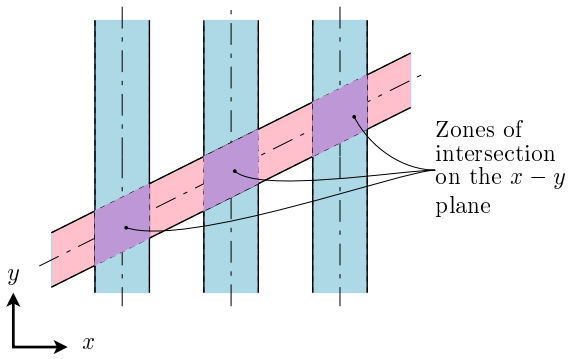

Figure 11: Zones of intersection of axial and bias tows in the $x-y$ plane.

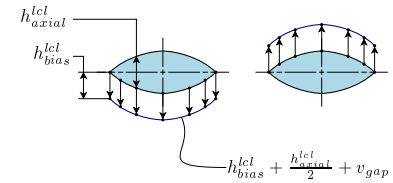

(a) Local height for offset surface definition

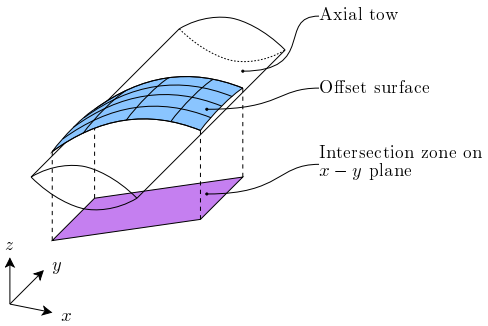

(b) Generated offset surface

Figure 12: Offset surface generation.

Once the initial distribution is obtained and the geometry is considered to be feasible, we can define different zones for the bias tows. Projected on the $x-y$ plane we can identify zones of intersection between the axial and bias tows, as shown in Fig. 11. Starting from the intersection areas, corresponding offset surfaces are built. The construction of the offset surfaces is done by obtaining at each point (x, y) inside the intersection area a local height of the bias tow h^{lcl}_{bias} and adding it to the local height of the axial tow h^{lcl}_{axial}. The imposed vertical gap v_{gap} between tows is added to the final value, as shown in Fig. 12a. The generated surface has a projection on the $x-y$ plane equal to the zone of intersection shown in Fig. 11 and also shown in Fig. 12b.

With the offset surfaces, an initial geometry can be built. For simplicity, 3 surfaces are built, as shown in Fig. 13a:

Surface A: over the surface of the left axial tow, between its central axis and its rightmost border.

Surface B: between the rightmost border of the left axial tow and leftmost border of the right axial tow.

Surface C: over the surface of the right axial tow, between its leftmost border and its central axis.

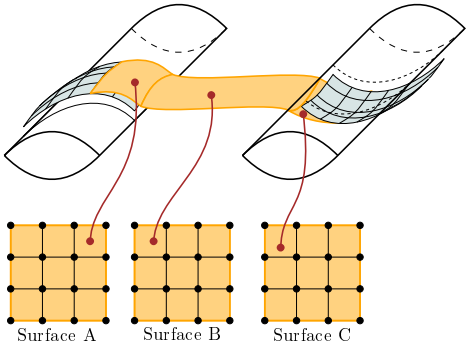

(a) Surfaces separation.

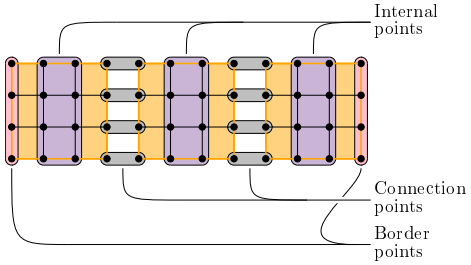

(b) Points classification.

Figure 13: Surface division and points classification

The control points of all the surfaces are classified, as shown in Fig. 13b, and treated separately:

Border points: they are modified initially, such that surfaces A and C follow the offset surfaces.

Internal points: they are modified by minimizing the length of the surface, such that the area is minimal. The requirement is that the surface is minimal and that there is no penetration between tows.

Connection points: they are modified in such a way that surfaces A and B are tangent, and surfaces B and C are tangent.

2.2.3. Area Minimization

The area minimization problem can be written as a minimization problem with inequality constraints, such that the area of the surface is minimal and that there is no interpenetration between the bias tows.

The interpenetration points are a set of points, distributed in the intersection area between two bias tows, as shown in Fig. 14a. To enforce tangency between surfaces in the case where surface B touches the border of the offset reference surface, tangency constraint points are obtained on the border, tangent to the surface at a distance d_{tng}, as shown in Fig. 14b.

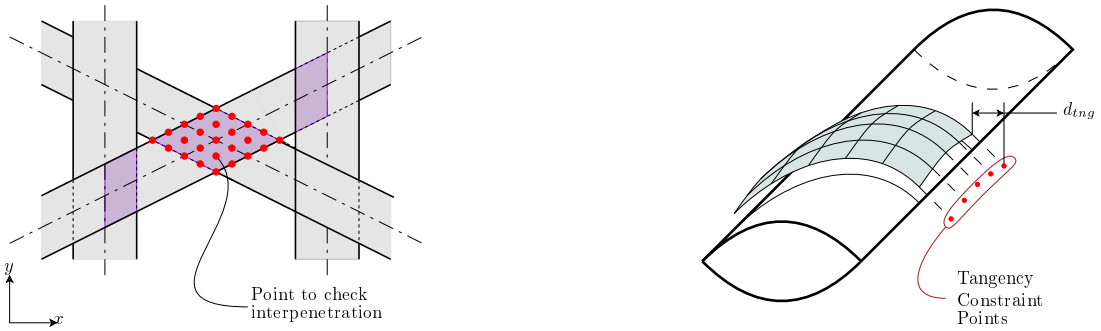

(a) Interpenetration points

(b) Tangency points

Figure 14: Constraint points

The minimization problem is written as

$$\begin{aligned} \min \quad & \mathcal{A}\,, \\ \text{s.t.} \quad & \Delta_i^p \geq 0 \\ & \Delta_j^t \geq 0 \end{aligned} \tag{12}$$

where $\mathcal{A}$ is the area to be minimized, Δ_i^p is the distance in the z direction between the interpenetration control points and Δ_j^t is the distance in the z direction between the surface and the tangency constraints

points. Introducing slack variables s_i and t_j, the system is rewritten

$$\begin{aligned} \min \quad & \mathcal{A}\,. \\ \text{s.t.} \quad & \Delta_i^p - {s_i}^2 = 0 \\ & \Delta_j^t - {t_j}^2 = 0 \end{aligned} \tag{13}$$

In order to conduct the minimization, we define the Lagrangian as

$$\mathcal{L} = \mathcal{A} + \sum_{i=1}^{n_P} \lambda_i \left(\Delta_i^p - {s_i}^2\right) + \sum_{j=1}^{n_T} \theta_j \left(\Delta_j^t - {t_j}^2\right) , \tag{14}$$

where n_P is the number of interpenetration points to be verified, λ_i are the Lagrange multipliers for the interpenetration constraint, Δ_i^p is the distance between the tow surfaces, n_T is the number of points to check to ensure tangency when surface B touches the border of the offset reference surface.

The functional $\mathcal{A}$ representing the surface area is highly non-linear and difficult to handle. To simplify the problem, as suggested by Nitsche [53], instead of using the surface area, we use the Dirichlet's energy $\mathcal{D}$. Following the work of Monterde [54], we obtain an explicit expression for the derivative of the Dirichlet functional with respect to the coordinates of the control points of the Bézier surfaces, with

$$\mathcal{L} = \mathcal{D} - \sum_{i=1}^{n_P} \lambda_i \left(\Delta_i^p - {s_i}^2\right) - \sum_{j=1}^{n_T} \theta_j \left(\Delta_j^t - {t_j}^2\right) . \tag{15}$$

The problem of minimizing the Lagrangian $\mathcal{L}$ consists in writing the minimization problem as a quasi Newton problem as

$$Z^{k+1} = Z^k - \mathbf{H}^{k^{-1}} G^k , \tag{16}$$

where Z^k is the vector of coordinates z of each control point of the Bézier surface, G is a vector of the derivatives of $\mathcal{L}$ and $\mathbf{H}$ is the Hessian matrix of $\mathcal{L}$

$$G = \begin{Bmatrix} \partial_z \mathcal{L} \\ \partial_\lambda \mathcal{L} \\ \partial_s \mathcal{L} \\ \partial_\theta \mathcal{L} \\ \partial_t \mathcal{L} \end{Bmatrix} , \tag{17}$$

$$\mathbf{H} = \begin{bmatrix} \partial^2_{zz}\mathcal{L} & \partial^2_{z\lambda}\mathcal{L} & \partial^2_{zs}\mathcal{L} & \partial^2_{z\theta}\mathcal{L} & \partial^2_{zt}\mathcal{L} \\ \partial^2_{\lambda z}\mathcal{L} & \partial^2_{\lambda\lambda}\mathcal{L} & \partial^2_{\lambda s}\mathcal{L} & \partial^2_{\lambda\theta}\mathcal{L} & \partial^2_{\lambda t}\mathcal{L} \\ \partial^2_{sz}\mathcal{L} & \partial^2_{s\lambda}\mathcal{L} & \partial^2_{ss}\mathcal{L} & \partial^2_{s\theta}\mathcal{L} & \partial^2_{st}\mathcal{L} \\ \partial^2_{\theta z}\mathcal{L} & \partial^2_{\theta\lambda}\mathcal{L} & \partial^2_{\theta s}\mathcal{L} & \partial^2_{\theta\theta}\mathcal{L} & \partial^2_{\theta t}\mathcal{L} \\ \partial^2_{tz}\mathcal{L} & \partial^2_{t\lambda}\mathcal{L} & \partial^2_{ts}\mathcal{L} & \partial^2_{t\theta}\mathcal{L} & \partial^2_{tt}\mathcal{L} \end{bmatrix} . \tag{18}$$

For a detailed development of the expressions, please refer to appendix Appendix A.

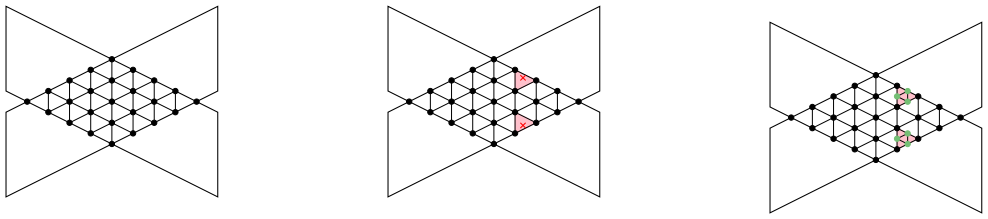

(a) Initial distribution of interpenetration points

(b) Minimum interpenetration point and triangle where it is located

(c) Triangles subdivision

Figure 15: Points refinement for effective interpenetration detection

The interpenetration points are distributed initially in a uniform way, such that some level of interpenetration can be detected and that the system to be minimized does not become ill-conditioned. This initial distribution approach can be insufficient to effectively detect and avoid interpenetration. To overcome this, a refinement can be applied. The first step is to have an initial, coarse distribution of points. This distribution of points is used to generate a triangle distribution, as shown in Fig. 15a. Considering this distribution, the surface minimization is performed and the point of minimum interpenetration is obtained as well as the triangle where it belongs to, as shown in Fig. 15b. Once the triangle is identified, it is subdivided into four triangles, as shown in Fig. 15c. This new points and triangles are subsequently used if the minimum interpenetration is below a given tolerance. This approach based on triangles subdivision prevents points from being too close to each-other, which could lead to an ill-conditioned system.

2.2.4. Sensitivity and Update

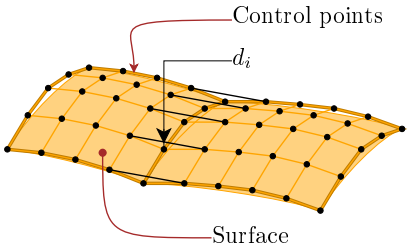

Figure 16: Straight segments between surfaces and vertical distances.

The sensitivity calculation is imposed on the connecting points (see gray points in Fig. 13b). To obtain a sensitivity that ensures tangency between the surfaces, the adjacent control points of the surfaces are connected by a straight segment, as shown in Fig. 16. The distance d_i between each straight segment and the surface is measured along the z direction. To obtain the sensitivity that allows a stable optimization, the functional to minimize is

$$F = \sum {d_i}^2 \,. \tag{19}$$

The sensitivity of F with respect to each control point z_j^C is calculated as

$$J_j = \frac{\partial F}{\partial z_j^C} = \sum 2d_i \frac{\partial z^S}{z_j^C}\,, \tag{20}$$

where z^S is the z coordinate on the surface. The control points z^C and point on the surface z^S are illustrated in figure 17.

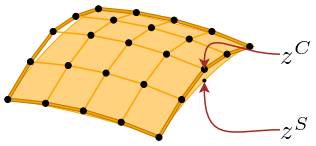

Figure 17: Point on surface z^S and control point z^C

The update of the control points is performed using a scheme that considers an inexact line search. To this end, in order to perform a multidimensional optimization of the cost function that ensures tangency between the surfaces, a 1D line search is performed at each iteration, in order to obtain a step size α that minimizes the problem in a given direction. The update is performed as

$$\mathbf{z}^{(k+1)} = \mathbf{z}^{(k)} - \alpha \mathbf{J}^{(k)}\,. \tag{21}$$

where $\mathbf{z}$ is the vector formed by terms z_j^C and $\mathbf{J}$ is the vector formed by terms $J_j = \frac{\partial F}{\partial z_j^C}$.

Usually, exact line search methods are preferred, but they can be numerically expensive, as they require several evaluations of the function. The approach used here is an adaptation of the Gradient-only line searches by Kafka and Wilke [55]. The calculation is performed as

1. At a given point $\mathbf{z}^{(k)}$ the gradient $\mathbf{J}^{(k)}$ is evaluated.
2. A new point $\mathbf{z}^{(k+1)}$ is calculated.
   - If $\left\langle \mathbf{J}^{(k)}, \mathbf{J}^{(k+1)} \right\rangle \geq 0$, the point $\mathbf{z}_{(k+1)}$ is valid. It is set as the new given point. The step size is updated as $\alpha \leftarrow \alpha \times \beta$.
   - If $\left\langle \mathbf{J}^{(k)}, \mathbf{J}^{(k+1)} \right\rangle < 0$, the point $\mathbf{z}_{(k+1)}$ is not valid. The step size is updated as $\alpha \leftarrow \alpha/\beta$ and the point $\mathbf{z}^{(k+1)}$ is recalculated.

   where β is a scalar such that $\beta > 1.0$.

The present work introduces a constrained optimization in order to obtain a compatible shape of of the bias tows by minimizing the central surface area and removing the interpenetration of the tows. Depending on the combination realization of the geometrical parameters, some geometries are not physically achievable (an example of unphysical geometries would be when axial tows have a width w_{axial} larger than the axial separation s_{axial}.), while for the ones achievable the generator is able to provide a RUC geometry as it will be discussed in the next Section 3.

3. Examples and Results

This section first presents the benchmark used as base for verification and validation of the generation method and subsequently the robustness of the generation method.

3.1. Benchmark

The benchmark is a regular pattern, with a braiding angle of 60° was chosen in order to conduct a comparison against the experimental and numerical results provided by Catera et al. [56]. The geometrical parameters of the model are reported in Table 1, the mechanical properties of the fibers in Table 2 and the mechanical properties of the resin in Table 3. The geometrical properties were extracted from the RUC information provided by Catera et al. [56], and the mechanical properties are the same as reported by Catera et al. [56]. This example is developed for a regular pattern with cover factor close to 1.

Table 1: Geometrical parameters of braid (evaluated from RUC data reported by Catera et al. [56]).

Parameter	w_{axial}	h_{axial}	w_{bias}	h_{bias}	s_{axial}	v_{gap}
Value [mm]	5.500	0.278	3.700	0.210	9.040	0.0083

Table 2: Material properties of T700S carbon reported by fibers Catera et al. [56].

Longitudinal Modulus	[GPa]	230
Transverse Modulus	[GPa]	15
Longitudinal Shear Modulus		24
Transverse Shear Modulus		5.03
Longitudinal-Transverse Major Poisson's ratio		0.27
Transverse-Transverse Poisson's ratio		0.49
Density	[g·/cm^{-3}]	1.8

Table 3: Material properties of E862 epoxy resin reported by Catera et al. [56].

Elastic Modulus	[GPa]	2.7
Shear Modulus	[GPa]	1
Elastic Poisson's ratio		0.35
Density	[g·cm^{-3}]	1.2

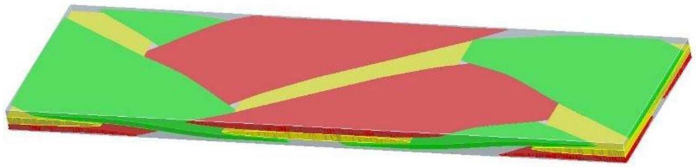

(a) RUC obtained by Catera et al. [56].

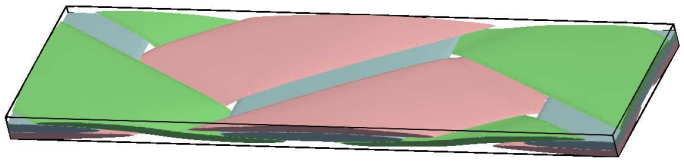

(b) RUC obtained by the current method.

Figure 18: Comparison of generated RUC: (a) Following [56] and reprinted from "Composite Structures, Piervincenzo Giovanni Catera, Francesco Gagliardi, Domenico Mundo, Luigi De Napoli, Anna Matveeva, Laszlo Farkas, Multi-scale modeling of triaxial braided composites for FE-based modal analysis of hybrid metal-composite gears, Volume 182, Pages 116-123, Copyright (2017), with permission from Elsevier"; and (b) As generated with the present method.

3.1.1. Generated RUC geometry assessment

The generated geometry for the given geometrical parameters is shown in Fig. 18 where it is visually compared to a RUC generated by Catera et al. [56]. A qualitative comparison of the generated cross sections is then performed against the micro-graphs obtained by Byun [18], see Fig. 18. It can be observed that the shapes are similar, but there are differences due to the lack of compression in the z direction in the simulation and that is present in the manufacturing of the experimental sample. This compression deforms the tows and they become variable along the tows.

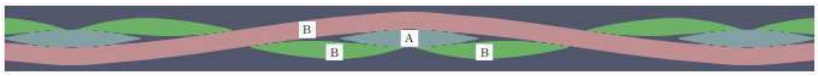

(a) Slice taken along a bias tow, as in the current simulation

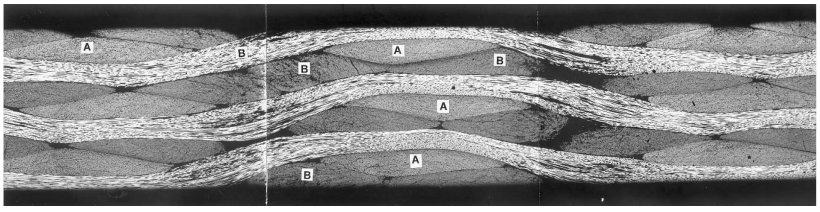

(b) Slice taken along a bias tow, obtained from Byun [18]

Figure 19: Cross sections along one bias tow: (a) As generated with the present method; and Following [18] and reprinted from "Composites Science and Technology,Joon-Hyung Byun, The analytical characterization of 2-D braided textile composites, Volume 60, Issue 5, Pages 705-716, Copyright (2000), with permission from Elsevier".

3.1.2. Generated RUC homogenized properties assessment

The mechanical properties are obtained by performing a 2-step homogenization: one step to predict the tows properties, going from the micro-scale to the meso-scale by considering an homogenization of the fibers and the resin in the yarns, and another step going from the meso-scale to the macro-scale, considering the homogenized tows as components to homogenize with the resin.

Homogenized Properties of the yarns. The micro-meso homogenization is achieved analytically using Chamis [25] fomulas:

$$\rho = V_f \cdot \rho_F + (1 - V_f) \cdot \rho_m \,, \tag{22}$$

$$E_L = V_f \cdot E_{LF} + (1 - V_f) \cdot E_m \,, \tag{23}$$

$$E_T = \frac{E_m}{1 - \sqrt{V_f} \cdot \left(1 - \frac{E_m}{E_{TF}}\right)} \,, \tag{24}$$

$$G_{LT} = \frac{G_m}{1 - \sqrt{V_f} \cdot (1 - G_m / G_{LTF})} \,, \tag{25}$$

$$G_{TT} = \frac{G_m}{1 - \sqrt{V_f} \cdot (1 - G_m / G_{TTF})} \,, \tag{26}$$

$$\nu_{TT} = \frac{E_T}{2 \cdot G_{TT}} - 1 \,, \tag{27}$$

$$\nu_{LTmajor} = V_f \cdot \nu_{LTF} + (V_f - 1) \cdot \nu_m \,, \tag{28}$$

$$\nu_{TLminor} = \nu_{LTmajor} \cdot \frac{E_T}{E_L} \,, \tag{29}$$

where ρ is the density, E_L is the longitudinal Young's modulus, E_T is the transverse Young's modulus, ν_{TT} is the Poisson's ratio, $\nu_{LTmajor}$ is the major longitudinal-transverse Poisson's ratio, $\nu_{TLminor}$ is the minor longitudinal-transverse Poisson's ratio. The resulting values are reported in Table 4 when considering a volume fraction $V_f = 0.86$ as suggested by of Catera et al. [56].

Table 4: Homogenized properties of the yarns for $V_f = 0.86$.

ρ	E_L	E_T	G_{LT}	G_{TT}	ν_{TT}	$\nu_{LTmajor}$	$\nu_{TLminor}$
[g·mm^{-3}]	[GPa]	[GPa]	[GPa]	[GPa]			
1716	198.2	11.27	8.98	3.87	0.45	0.31	0.017

Homogenized Properties of the RUC. The homogenized properties are obtained using the finite element method and applying periodic boundary conditions. The homogenized material operator is obtained following the approach suggested by Nguyen et al. [57]. The properties of the tows being orthotropic, they follow the generated directions as shown in Fig. 20. The results using the current method are compared against the numerical and experimental results of Catera et al. [56] in Table 5, where a good agreement with the experimental results can be seen.

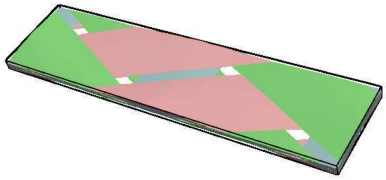

(a) Generated tow volumes

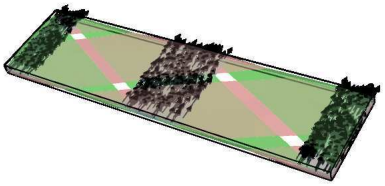

(b) Inside the axial tow volumes

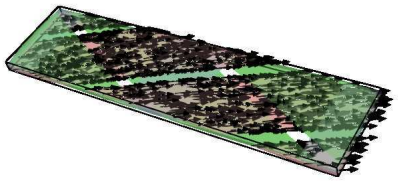

(c) Inside the bias tow volumes

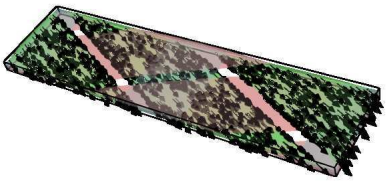

(d) Inside the bias tow volumes

Figure 20: Directions of points in the axial and bias tows of the benchmarked regular RUC obtained by the current method.

Table 5: Results comparison of current method against Catera et al. [56]

	E_x [GPa]	E_y [GPa]	E_z [GPa]	ν_{xy}	ν_{yz}	ν_{xz}
Catera et al. [56] (exp.)	40.6	38.5	-	-	-	-
Catera et al. [56] (num.)	42.8	41.4	7.40	0.3	0.39	0.36
Current (num.)	42.7	42.6	7.05	0.29	0.36	0.35

3.2. Two-parameter robustness study

The robustness of the generation method is studied by changing the geometrical parameters from the base model by a random amplitude and running a batch of simulations. The robustness refers to the capability of the algorithm to effectively generate RUCs for different sets of compatible geometrical parameters, *i.e.* sets of parameters that do not lead to unphysical overlaps of the tows, including for combinations of geometrical parameters of the RUC which result in high cover factors C_f, i.e. close to the unity. An example of unphysical overlap is for axial tows whose width w_{axial} is larger than the axial separation s_{axial}. The chosen parameters for this robustness study are the axial tow separation s_{axial} and the braiding angle θ, with a random amplitude of ± 5 [mm] and $\pm 5[^\circ]$ respectively. The cross section of the tows is elliptical.

3.2.1. Diamond Pattern

The parameters of the base model for the diamond pattern are shown in Table 6. The braiding angle is $45[^\circ]$. The generated tow volumes, as well as a figure showing the directions of the points inside the bias tows for the base model can be seen in Fig. 21. Fig. 22 depicts the validity of the generated RUCs for different combinations of the parameters. It can be seen that high cover factors close to one can be achieved. In this figure, the black line dividing the plane represents a cover factor of $1 - 1e - 10$. For the

Table 6: Base parameters for the two-parameter robustness study of the diamond pattern generation

Parameter	w_{axial}	h_{axial}	w_{bias}	h_{bias}	v_{gap}	s_{axial}	θ
Unit	[mm]	[mm]	[mm]	[mm]	[mm]	[mm]	[°]
Value	4.00	0.50	4.0	0.50	0.01	5.0	45
Deviation	-	-	-	-	-	±5.0	±5.0

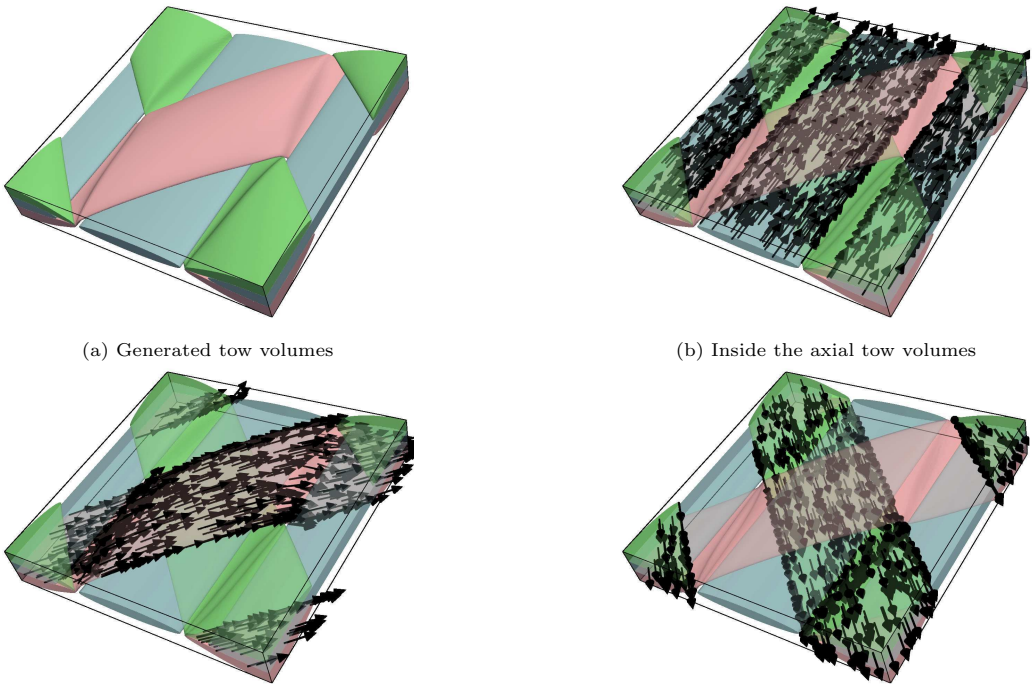

(a) Generated tow volumes

(b) Inside the axial tow volumes

(c) Inside the bias tow volumes

(d) Inside the bias tow volumes

Figure 21: Generated base diamond RUC for the two-parameter robustness study

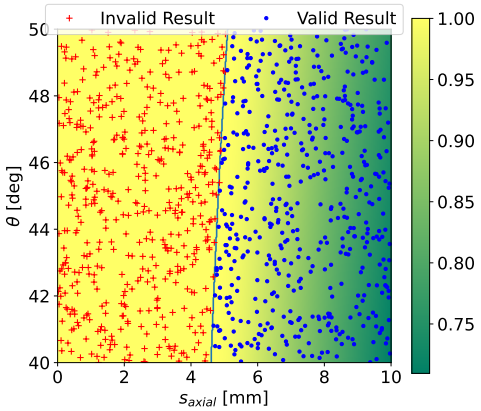

Figure 22: Two-parameter robustness assessment of the geometry generation for the diamond pattern

cases where the parameter combination is valid, two examples are shown in Fig. 23, and two examples of invalid combinations are shown in Fig. 24. In these examples, the projection on the $x-y$ plane of the tows and the generated volumes of the tows are shown. It is clear that the failure of the generator results from an physically impossible configuration to reach.

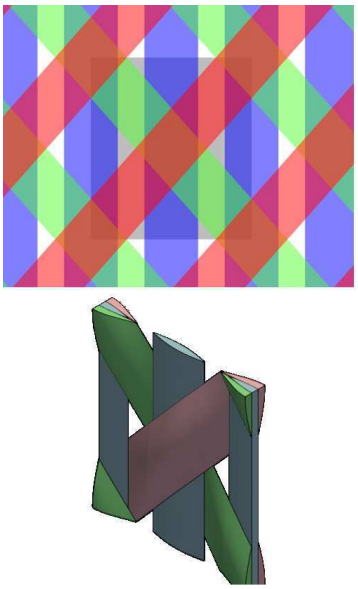

(a) $s_{axial} = 5.978$ [mm], $\theta = 45.23[^\circ]$, $C_f = 0.952$

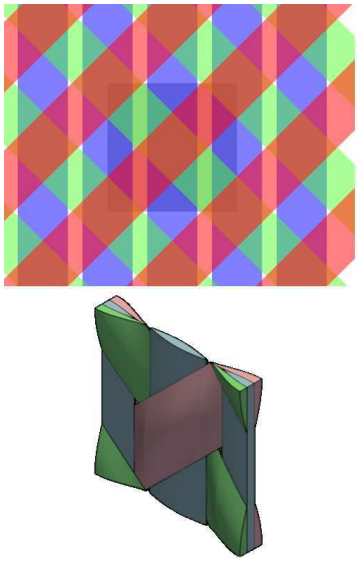

(b) $s_{axial} = 5.163$ [mm], $\theta = 40.20[^\circ]$, $C_f = 0.996$

Figure 23: Example of valid two-parameter combination for the generation of diamond pattern

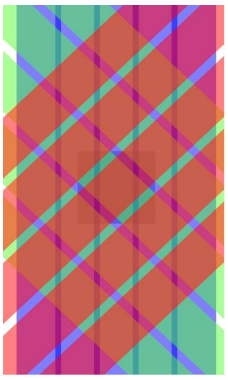

(a) $s_{axial} = 3.482$ [mm], $\theta = 46.75[^\circ]$

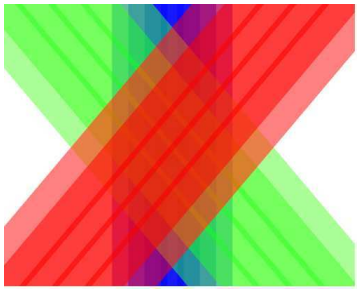

(b) $s_{axial} = 1.182$ [mm], $\theta = 40.20[^\circ]$

Figure 24: Example of invalid two-parameter combination for the generation of diamond pattern

3.2.2. Regular Pattern

The parameters of the base model for the regular pattern are reported in Table 7. The braiding angle is 60[°]. The generated tow volumes, as well as a figure showing the directions of the points inside the bias

Parameter	w_{axial}	h_{axial}	w_{bias}	h_{bias}	v_{gap}	s_{axial}	θ
Unit	[mm]	[mm]	[mm]	[mm]	[mm]	[mm]	[°]
Value	4.10	0.50	3.80	0.50	0.01	10.0	60.0
Deviation	-	-	-	-	-	±5.0	±5.0

Table 7: Base parameters for the two-parameter robustness study of the regular pattern generation

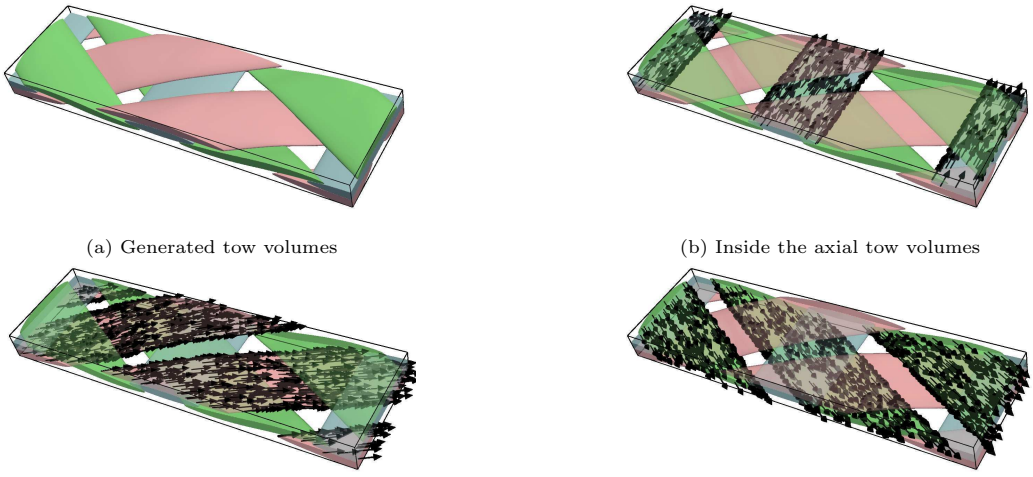

(a) Generated tow volumes

(b) Inside the axial tow volumes

(c) Inside the bias tow volumes

(d) Inside the bias tow volumes

Figure 25: Generated base regular RUC for the two-parameter robustness study

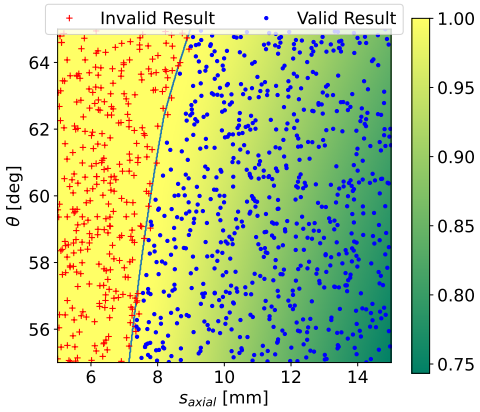

Figure 26: Two-parameter robustness assessment of the geometry generation for the regular pattern

tows can be seen in Fig. 25. Fig. 26 depicts the validity of the generated RUCs for different combinations of the parameters. As for the diamond pattern, high cover factors close to one can be achieved. In this figure, the black line dividing the plane represents a cover factor of $1 - 1e - 10$. For the cases where the parameter combination is valid, respectively invalid, two examples of generated RUC are shown in Fig. 27, respectively in Fig. 28. In these examples, only the projection on the $x - y$ plane of the tows is shown.

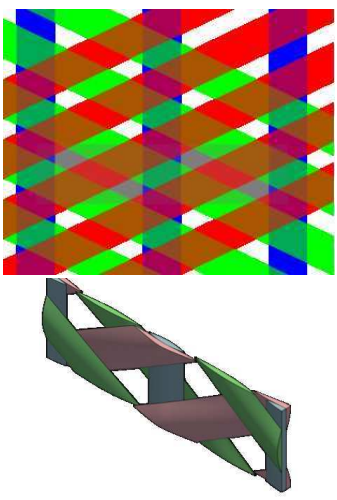

(a) $s_{axial} = 13.544$ [mm], $\theta = 64.54[^\circ]$, $C_f = 0.8906$

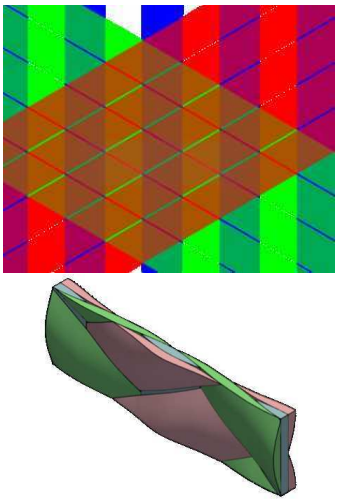

(b) $s_{axial} = 7.938$ [mm], $\theta = 59.88[^\circ]$, $C_f = 0.9996$

Figure 27: Example of valid two-parameter combination for the generation of regular pattern

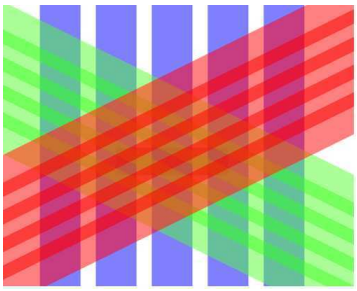

(a) 5.636 63.66 $s_{axial} = 3.482$ [mm], $\theta = 46.75[^\circ]$

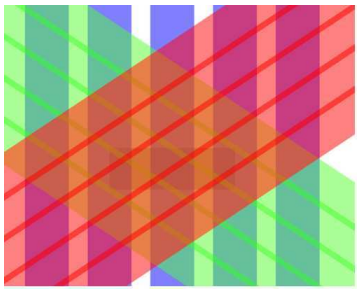

(b) 5.861 56.37$s_{axial} = 1.182$ [mm], $\theta = 40.20[^\circ]$

Figure 28: Example of invalid two-parameter combination for the generation of regular pattern

3.3. Multiple-parameter robustness study

The robustness of the generation method is now studied by changing all the geometrical parameters from the base model by a random amplitude and running a batch of simulations. The chosen parameters for this study are the axial tow separation s_{axial}, the braiding angle θ and the geometrical parameters of the cross section of the axial and bias tows w_{axial}, h_{axial}, w_{bias} and h_{bias}. The cross section of the tows is elliptical.

3.3.1. Diamond Pattern

The parameters of the base model for the diamond pattern are reported in Table 8. The braiding angle is $45[^\circ]$. To illustrate the validity of the generated geometries, keeping the random values for s_{axial}, θ, h_{axial}, h_{bias}, results for different combinations of w_{axial} and w_{bias} are shown in Fig. 29. A set of examples for each of the validity ranges shown in Fig. 29 is shown in Fig. 30, showing a wide range and different combinations for which the RUC can be generated.

Table 8: Base parameters for the multiple-parameter robustness study of the diamond pattern generation

Parameter	w_{axial}	h_{axial}	w_{bias}	h_{bias}	v_{gap}	s_{axial}	θ
Unit	[mm]	[mm]	[mm]	[mm]	[mm]	[mm]	[°]
Value	4.00	0.50	4.00	0.50	0.01	5.0	45
Deviation	±0.50	±0.05	±0.50	±0.05	-	±5.0	±5.0

3.3.2. Regular Pattern

Table 9: Base parameters for the multiple-parameter robustness study of the regular pattern generation

Parameter	w_{axial}	h_{axial}	w_{bias}	h_{bias}	v_{gap}	s_{axial}	θ
Unit	[mm]	[mm]	[mm]	[mm]	[mm]	[mm]	[°]
Value	4.10	0.50	3.80	0.50	0.01	10.0	60.0
Deviation	±0.50	±0.05	±0.50	±0.05	-	±5.0	±5.0

A set of examples for each of the validity ranges shown in figure 31 is shown in figure 32. It shows a wide range and different combinations that are possible to obtain.

The parameters of the base model for the regular pattern are reported in Table 9. The braiding angle is 60[°]. To illustrate the validity of the generated geometries, keeping the randmon values for s_{axial}, θ, h_{axial}, h_{bias}, results for different combinations of w_{axial} and w_{bias} are shown in Fig. 31, with some realizations reported in Fig. 32. As for the diamond pattern, a high cover factor can be reached for multiple combinations.

3.4. Computational Cost

For illustrative purposes, the computational costs of the generation and finite-element resolution, through a condensation step [57], of realizations of the regular pattern, *i.e.* for different sets of geometrical parameters covered by the two-parameter sensitivity study, are now discussed.

The simulations were performed on the cluster "Lemaitre 4", which is part of the "Consortium des Équipements de Calcul Intensif" (CECI), in Belgium. This cluster consists of more than 5000 cores AMD Epyc Genoa at 3.7 GHz. All the nodes are interconnected by a 100 Gbps Infiniband HDR interconnect. The nodes have access to a 320 TB fast BeeGFS /scratch space. The simulations were performed on a single core, in an "Embarrassingly parallel / Job array" manner, which means that they were run in parallel but each on a single core.

The resources are categorized into "Geometry and mesh generation" and "Geometry and mesh generation, with finite element condensation" and are reported in Table 10.

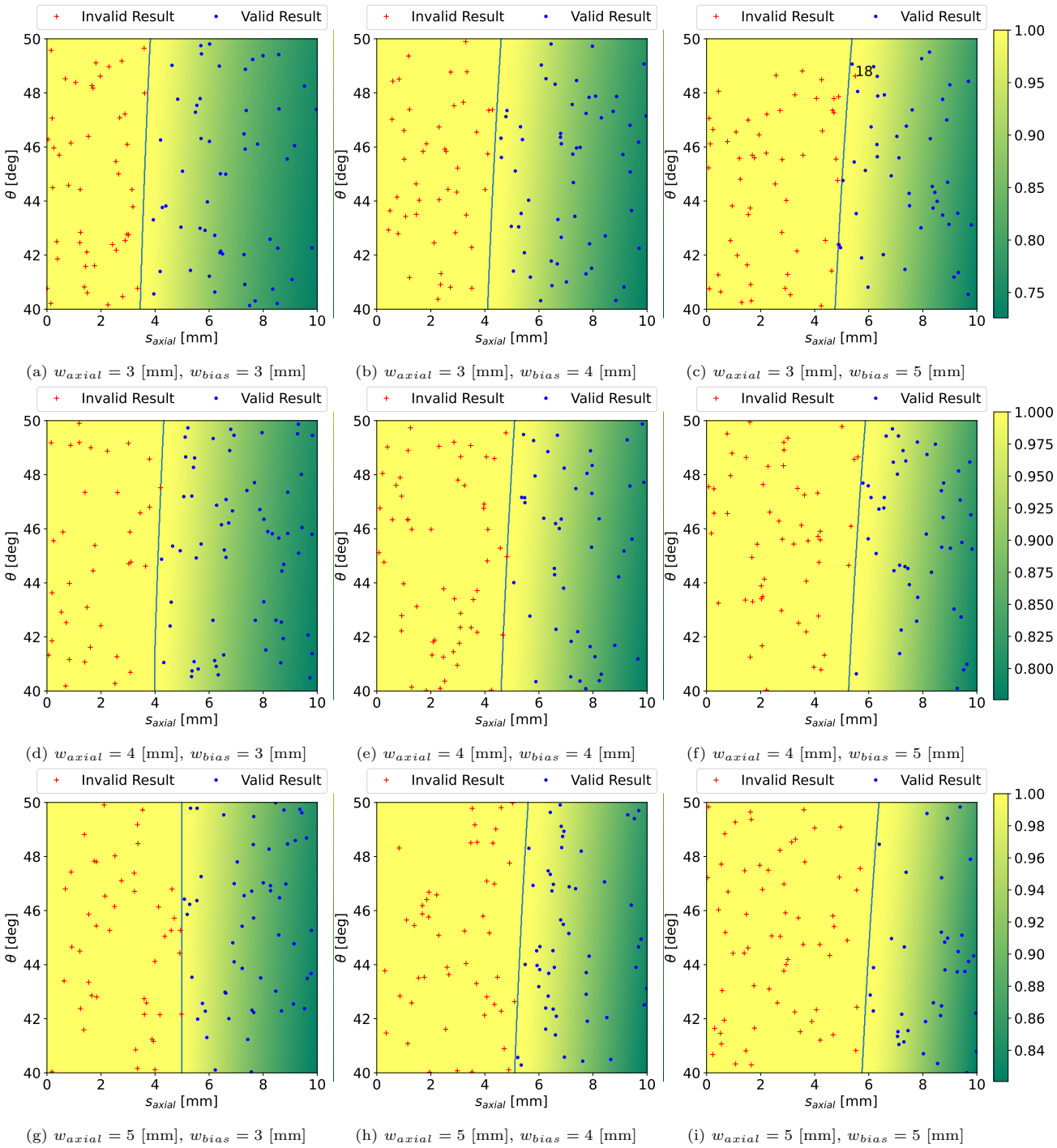

(a) $w_{axial} = 3$ [mm], $w_{bias} = 3$ [mm] (b) $w_{axial} = 3$ [mm], $w_{bias} = 4$ [mm] (c) $w_{axial} = 3$ [mm], $w_{bias} = 5$ [mm]

(d) $w_{axial} = 4$ [mm], $w_{bias} = 3$ [mm] (e) $w_{axial} = 4$ [mm], $w_{bias} = 4$ [mm] (f) $w_{axial} = 4$ [mm], $w_{bias} = 5$ [mm]

(g) $w_{axial} = 5$ [mm], $w_{bias} = 3$ [mm] (h) $w_{axial} = 5$ [mm], $w_{bias} = 4$ [mm] (i) $w_{axial} = 5$ [mm], $w_{bias} = 5$ [mm]

Figure 29: Multiple-parameter robustness assessment of the geometry generation for the diamond pattern illustrated for different combinations of w_{axial} and w_{bias}

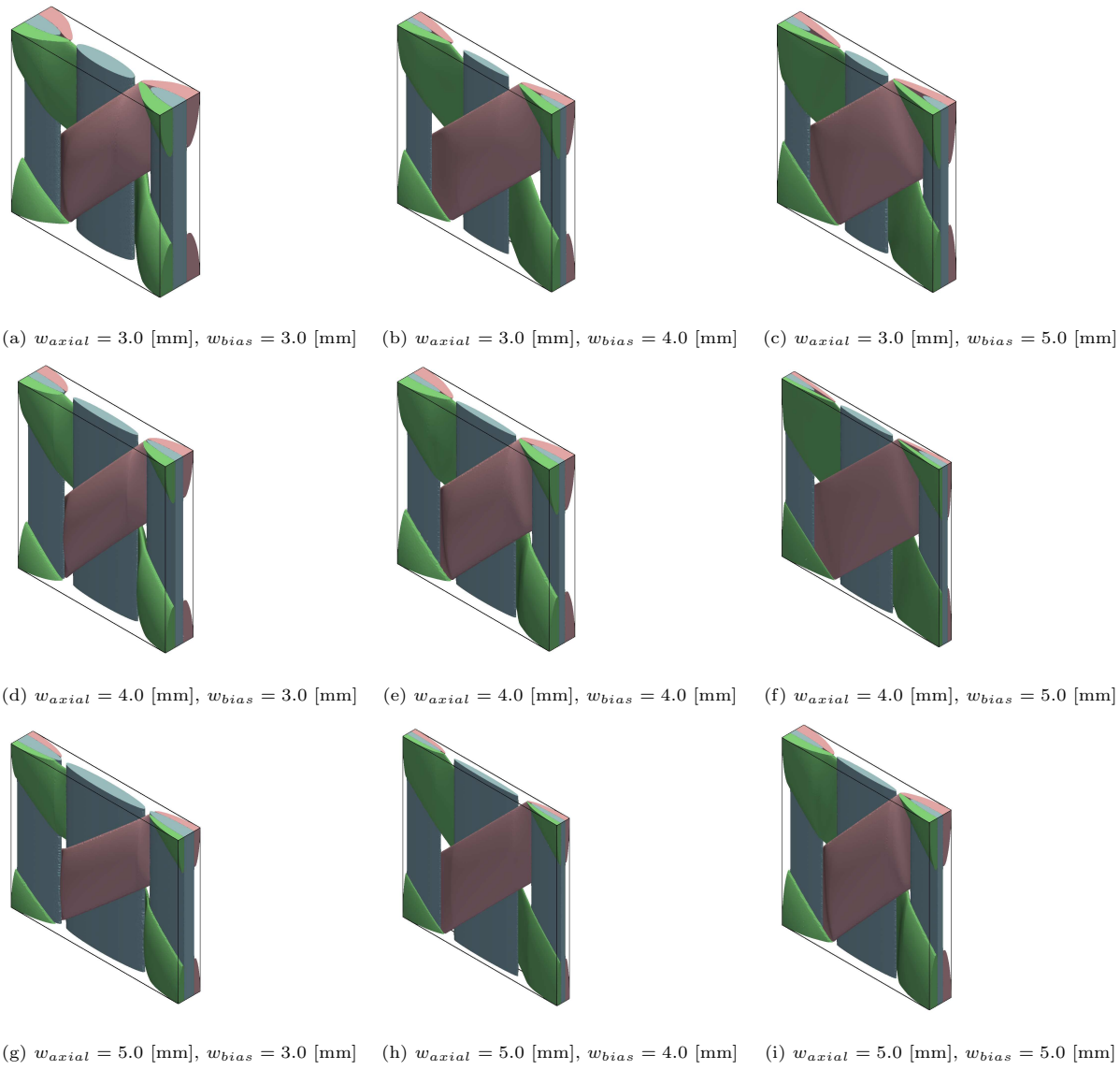

(a) $w_{axial} = 3.0$ [mm], $w_{bias} = 3.0$ [mm] (b) $w_{axial} = 3.0$ [mm], $w_{bias} = 4.0$ [mm] (c) $w_{axial} = 3.0$ [mm], $w_{bias} = 5.0$ [mm]

(d) $w_{axial} = 4.0$ [mm], $w_{bias} = 3.0$ [mm] (e) $w_{axial} = 4.0$ [mm], $w_{bias} = 4.0$ [mm] (f) $w_{axial} = 4.0$ [mm], $w_{bias} = 5.0$ [mm]

(g) $w_{axial} = 5.0$ [mm], $w_{bias} = 3.0$ [mm] (h) $w_{axial} = 5.0$ [mm], $w_{bias} = 4.0$ [mm] (i) $w_{axial} = 5.0$ [mm], $w_{bias} = 5.0$ [mm]

Figure 30: Multiple-parameter robustness assessment: generated volumes for different combinations of w_{axial} and w_{bias}, diamond pattern

4. Conclusions and Remarks

In this article a novel method for the generation of representative unit cells of braided composites has been presented. The tows' geometry is generated with geometrical relations based on the surface minimization solving the Dirichlet problem. The use of Bézier surfaces is an original approach to represent the geometry of the tows, as compared to other geometrically-based generators which impose the shape as being a combination of sinusoidal and line functions. The geometry is then obtained as a result of a surface minimization instead of being *a priori* defined by the user. This results in an improved robustness of the

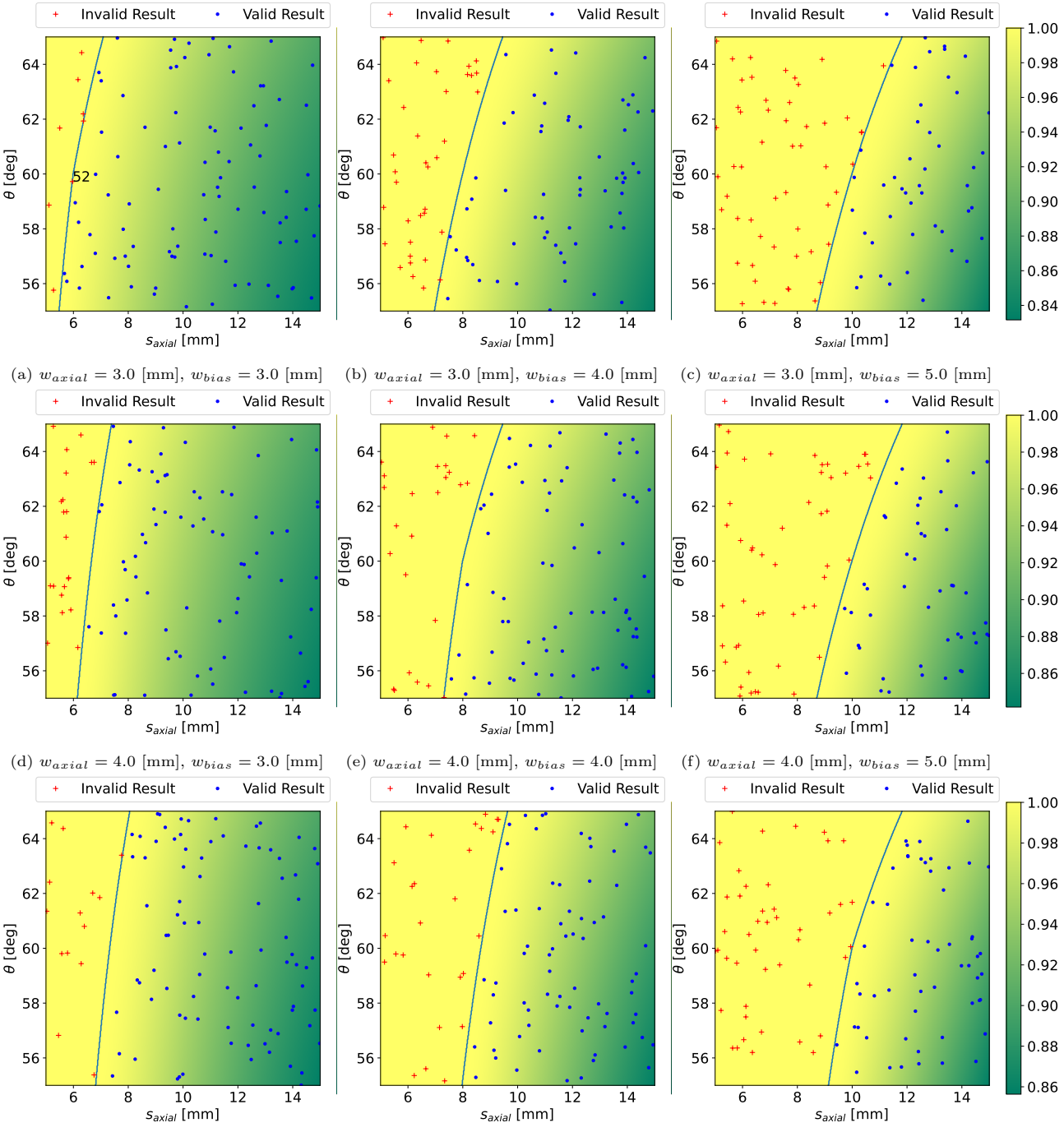

(a) $w_{axial} = 3.0$ [mm], $w_{bias} = 3.0$ [mm] (b) $w_{axial} = 3.0$ [mm], $w_{bias} = 4.0$ [mm] (c) $w_{axial} = 3.0$ [mm], $w_{bias} = 5.0$ [mm]

(d) $w_{axial} = 4.0$ [mm], $w_{bias} = 3.0$ [mm] (e) $w_{axial} = 4.0$ [mm], $w_{bias} = 4.0$ [mm] (f) $w_{axial} = 4.0$ [mm], $w_{bias} = 5.0$ [mm]

(g) $w_{axial} = 5.0$ [mm], $w_{bias} = 3.0$ [mm] (h) $w_{axial} = 5.0$ [mm], $w_{bias} = 4.0$ [mm] (i) $w_{axial} = 5.0$ [mm], $w_{bias} = 5.0$ [mm]

Figure 31: Multiple-parameter robustness assessment of the geometry generation for the regular pattern illustrated for different combinations of w_{axial} and w_{bias}.

generation process since the parameters that define the geometry of the volumes of the tows are obtained via the calculation of a minimal surface instead of being imposed. The generated geometry is eventually

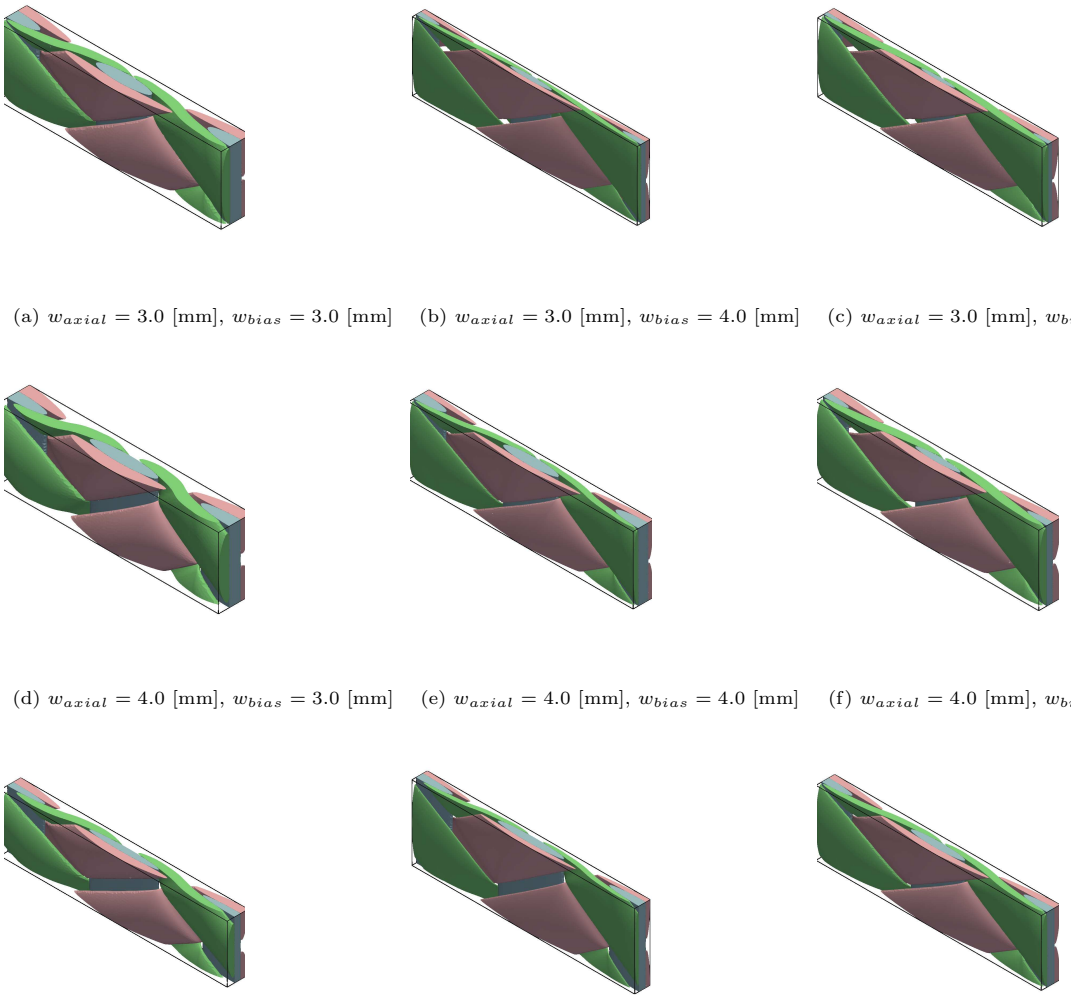

(a) $w_{axial} = 3.0$ [mm], $w_{bias} = 3.0$ [mm] (b) $w_{axial} = 3.0$ [mm], $w_{bias} = 4.0$ [mm] (c) $w_{axial} = 3.0$ [mm], $w_{bias} = 5.0$ [mm]

(d) $w_{axial} = 4.0$ [mm], $w_{bias} = 3.0$ [mm] (e) $w_{axial} = 4.0$ [mm], $w_{bias} = 4.0$ [mm] (f) $w_{axial} = 4.0$ [mm], $w_{bias} = 5.0$ [mm]

(g) $w_{axial} = 5.0$ [mm], $w_{bias} = 3.0$ [mm] (h) $w_{axial} = 5.0$ [mm], $w_{bias} = 4.0$ [mm] (i) $w_{axial} = 5.0$ [mm], $w_{bias} = 5.0$ [mm]

Figure 32: Multiple-parameter robustness assessment: generated volumes for different combinations of w_{axial} and w_{bias}, regular pattern

used to obtain a finite element model and to calculate orthotropy direction of the tows. The implementation is performed in Python using the GMSH API, which allows for a monolithic implementation.

In order to evaluate the homogenized properties of the RUC, a 2-step homogenization is conducted. The homogenization of the yarns is solved using Chamis equations and the homogenization of the cell is solved using the finite element method. The finite element model of the RUC considers an isotropic behavior of the matrix and an orthotropic behavior of the tows. The tows orthotropy direction is used to calculate orthotropic properties of the tows, depending on the material point location.

Table 10: Computational resources

Geometry and mesh generation				
Resource	minimum	mean	maximum	Std. Deviation
CPU Time[s]	3698	4882.21	14776	995.1
Memory [MB]	0.88	903.06	1085.66	86.74
Geometry and mesh generation, with finite element condensation				
Resource	minimum	mean	maximum	Std. Deviation
CPU Time[s]	4093	8966.25	27423	3181.14
Memory [MB]	3.61	8830.06	20747.35	3627.76

The method presented here has been tested for a certain range of geometrical values and has shown to be robust enough to model the geometry without user intervention, for both diamond and regular braiding patterns

In the future, the robustness of the method will allow to generate geometries automatically when considering the variability in the geometrical parameters, such as the braiding angle and axial tow separation. In this context, the automatic generation of the RUC is intended to be used to generate a set of homogenized properties as a synthetic database that can be used to train an artificial network (ANN). This ANN will in turn be used to obtain the macroscale mechanical properties of a mechanical component at reduced cost for given geometrical parameters, allowing for component or process optimization. In such a design methodology, the braiding angle and other geometrical parameters can be predicted using the methods developed by Du and Popper [58] and van Ravenhorst and Akkerman [59], *e.g.* whose description is beyond the scope of the present work.

Acknowledgments

The research has been funded by the Walloon Region under the agreement no.8422-SW_ViBra in the context of the 28th SKYWIN call.

Computational resources have been provided by the Consortium des Équipements de Calcul Intensif (CÉCI), funded by the Fonds de la Recherche Scientifique de Belgique (F.R.S.-FNRS) under Grant No. 2.5020.11 and by the Walloon Region.

Data availability

The code and raw/processed data required to reproduce these findings is available on `https://gitlab.onelab.info/cm3/cm3Braiding` [60] under the Creative Commons Attribution 4.0 International (CC BY

4.0) licence

Appendix A. Bezier Surface Minimization: Expanded Expressions

The Bezier surface is expressed as

$$\mathbf{x}(u,v) = \sum_{i=0}^{n}\sum_{j=0}^{m} B_i^n(u)\, B_j^m(v)\, \mathbf{P}_{ij} \tag{A.1}$$

where u and v are the local coordinates of the Bezier surface, $B_i^n(u)$ and $B_j^m(v)$ are the Bernstein polynomials and $\mathbf{P}_{ij}$ are the control points.

The expression of the Dirichlet energy $\mathcal{D}$, as used by Monterde [54], is

$$\mathcal{D} = \int_\Omega \|\mathbf{x}_u\|^2 + \|\mathbf{x}_v\|^2 \mathrm{d}u\, \mathrm{d}v\,, \tag{A.2}$$

where $\mathbf{x}_u$ is the derivative of the surface point $\mathbf{x}$ with respect to local coordinate u and $\mathbf{x}_v$ is the derivative of the surface point $\mathbf{x}$ with respect to local coordinate v. The derivative of $\mathcal{D}$ with respect to the coordinates of the control points of the surface is provided in Monterde [54] will not be copied here.

As a recall from equation (14), the Lagrangian is expressed in terms of the Dirichlet energy $\mathcal{D}$ as

$$\mathcal{L} = \mathcal{D} - \sum_{i=1}^{n_P} \lambda_i \left(\Delta_i^p - {s_i}^2\right) - \sum_{j=1}^{n_T} \theta_j \left(\Delta_j^t - {t_j}^2\right)\,. \tag{A.3}$$

The terms of vector $\mathbf{G}$, as derived from equation (A.3) used in equation (17), are

$$G = \begin{Bmatrix} \partial_z \mathcal{L} \\ -\left(\Delta_i^p - {s_i}^2\right) \\ 2\lambda_i s_i \\ -\left(\Delta_j^t - {t_j}^2\right) \\ 2\theta_j t_j \end{Bmatrix}, \text{ with} \tag{A.4}$$

$$\partial_z \mathcal{L} = \frac{\partial \mathcal{D}}{\partial z_a} + \sum_{i=1}^{n_P} \lambda_i \frac{\partial \Delta_i^p}{\partial z_a} + \sum_{j=1}^{n_T} \theta_j \frac{\partial \Delta_j^t}{\partial z_a}\,, \tag{A.5}$$

where z_a is the z coordinate of control point with index a.

The terms of matrix $\mathbf{H}$, as derived from equation (A.3) used in equation (18), are

$$\mathbf{H} = \begin{bmatrix} \partial^2_{zz}\mathcal{L} & -\frac{\partial \Delta_i^p}{\partial z_a} & 0 & -\frac{\partial \Delta_i^t}{\partial z_a} & 0 \\ -\frac{\partial \Delta_i^p}{\partial z_b} & 0 & 2s_i & 0 & 0 \\ 0 & s_i & 2\lambda_i & 0 & 0 \\ -\frac{\partial \Delta_j^t}{\partial z_b} & 0 & 0 & 0 & 2t_j \\ 0 & 0 & 0 & 2t_j & 2\theta_j \end{bmatrix}, \text{ with} \tag{A.6}$$

$$\partial^2_{zz}\mathcal{L} = \frac{\partial^2 \mathcal{D}}{\partial z_a \partial z_b} - \sum_{i=1}^{n_p} \lambda_i \frac{\partial^2 \Delta_i^p}{\partial z_a \partial z_b} - \sum_{j=1}^{n_t} \theta_j \frac{\partial^2 \Delta_j^t}{\partial z_a \partial z_b}\,, \tag{A.7}$$

where z_a is the z coordinate of control point with index a and z_b is the z coordinate of control point with index b, I is the identity matrix.

References

[1] Andrew Craig Long. *Design and manufacture of textile composites*. Elsevier, 2005.

[2] J.P. Carey. Introduction to braided composites. In *Handbook of Advances in Braided Composite Materials*, pages 1–21. Woodhead Publishing, 2017. ISBN 978-0-08-100369-5. doi: https://doi.org/10.1016/B978-0-08-100369-5.00001-5.

[3] Takashi Ishikawa and Tsu-Wei Chou. Stiffness and strength behaviour of woven fabric composites. *Journal of Materials Science*, 17(11):3211–3220, 1982. doi: 10.1007/BF01203485. URL https://doi.org/10.1007/BF01203485.

[4] Takashi Ishikawa and Tsu-Wei Chou. Elastic behavior of woven hybrid composites. *Journal of Composite Materials*, 16 (1):2–19, 1982. doi: 10.1177/002199838201600101. URL https://doi.org/10.1177/002199838201600101.

[5] Takashi Ishikawa and Tsu-Wei Chou. In-plane thermal expansion and thermal bending coefficients of fabric composites. *Journal of Composite Materials*, 17(2):92–104, 1983. doi: 10.1177/002199838301700201. URL https://doi.org/10.1177/002199838301700201.

[6] Takashi Ishikawa and Tsu-Wei Chou. One-dimensional micromechanical analysis of woven fabric composites. *AIAA Journal*, 21(12):1714–1721, 1983. doi: 10.2514/3.8314. URL https://doi.org/10.2514/3.8314.

[7] Jenn-Ming Yang, Chang-Long Ma, and Tsu-Wei Chou. Fiber inclination model of three-dimensional textile structural composites. *Journal of Composite Materials*, 20(5):472–484, 1986. doi: 10.1177/002199838602000505. URL https://doi.org/10.1177/002199838602000505.

[8] N.K. Naik and P.S. Shembekar. Elastic behavior of woven fabric composites: I—lamina analysis. *Journal of Composite Materials*, 26(15):2196–2225, 1992. doi: 10.1177/002199839202601502. URL https://doi.org/10.1177/002199839202601502.

[9] N.K. Naik and P.S. Shembekar. Elastic behavior of woven fabric composites: Ii—laminate analysis. *Journal of Composite Materials*, 26(15):2226–2246, 1992. doi: 10.1177/002199839202601503. URL https://doi.org/10.1177/002199839202601503.

[10] N.K. Naik and P.S. Shembekar. Elastic behavior of woven fabric composites: Iii — laminate design. *Journal of Composite Materials*, 26(17):2522–2541, 1992. doi: 10.1177/002199839202601704. URL https://doi.org/10.1177/002199839202601704.

[11] C.J. Redman and C.D. Douglas. Theoretical prediction of the tensile elastic properties of braided composites. *International SAMPE symposium and exhibition (proceedings) 38*, page 719–727, 1993.

[12] Ivatury Raju and John Wang. Classical laminate theory models for woven fabric composites. *Journal of Composites Technology and Research*, 16:289–303, 10 1994.

[13] N.K. Naik and V.K. Ganesh. Prediction of on-axes elastic properties of plain weave fabric composites. *Composites Science and Technology*, 45(2):135–152, 1992. ISSN 0266-3538. doi: https://doi.org/10.1016/0266-3538(92)90036-3. URL https://www.sciencedirect.com/science/article/pii/0266353892900363.

[14] A. Aggarwal, S. Ramakrishna, and V. K. Ganesh. Predicting the in-plane elastic constants of diamond braided composites. *Journal of Composite Materials*, 35(8):665–688, 2001. doi: 10.1177/002199801772662046. URL https://doi.org/10.1177/002199801772662046.

[15] AF Kregers and Yu G Melbardis. Determination of the deformability of spatially reinforced composites by the method of averaging stiffnesses. *Mekh. Polim.*, 1:3–8, 1978.

[16] AF Kreger and GA Teters. Optimization of the structure of three-dimensionally reinforced composites in stability problems. *Mechanics of Composite Materials*, 15(1):64–69, 1979.

[17] AF Kreger and GA Teters. Use of averaging methods to determine the viscoelastic properties of spatially reinforced composites. *Mechanics of composite materials*, 15(4):377–383, 1980.

[18] Joon-Hyung Byun. The analytical characterization of 2-d braided textile composites. *Composites Science and Technology*, 60(5):705–716, 2000. ISSN 0266-3538. doi: https://doi.org/10.1016/S0266-3538(99)00173-6. URL https://www.sciencedirect.com/science/article/pii/S0266353899001736.

[19] Shu Ching Quek, Anthony M. Waas, Khaled W. Shahwan, and Venkatesh Agaram. Analysis of 2d triaxial flat braided textile composites. *International Journal of Mechanical Sciences*, 45(6):1077–1096, 2003. ISSN 0020-7403. doi: https://doi.org/10.1016/j.ijmecsci.2003.09.003. URL https://www.sciencedirect.com/science/article/pii/S0020740303001632.

[20] Mahmood M. Shokrieh and Mohammad S. Mazloomi. An analytical method for calculating stiffness of two-dimensional tri-axial braided composites. *Composite Structures*, 92(12):2901–2905, 2010. ISSN 0263-8223.

[21] Rani F. El-Hajjar, Seyedmohammad S. Shams, and David J. Kehrl. Closed form solutions for predicting the elastic behavior of quasi-isotropic triaxially braided composites. *Composite Structures*, 101:1–8, 2013. ISSN 0263-8223.

[22] Zachary T. Kier, Amit Salvi, Geoffrey Theis, Anthony M. Waas, and Khaled Shahwan. Estimating mechanical properties of 2d triaxially braided textile composites based on microstructure properties. *Composites Part B: Engineering*, 68:288–299, 2015. ISSN 1359-8368. doi: https://doi.org/10.1016/j.compositesb.2014.08.039. URL https://www.sciencedirect.com/science/article/pii/S1359836814003771.

[23] Simon Heide-Jørgensen, Michal K. Budzik, and Claus H. Ibsen. Three-dimensional, multiscale homogenization for hybrid woven composites with fiber-matrix debonding. *Composites Science and Technology*, 218:109204, 2022. ISSN 0266-3538. doi: https://doi.org/10.1016/j.compscitech.2021.109204. URL https://www.sciencedirect.com/science/article/pii/S0266353821005601.

[24] John C Halpin. Effects of environmental factors on composite materials. Technical report, Air Force Materials Lab Wright-Patterson AFB OH, 1969.

[25] Christos C Chamis. Simplified composite micromechanics equations for hygral, thermal and mechanical properties. Technical Report NASA-TM-83320, NASA, 1983.

[26] Xinran Xiao, Hamid G. Kia, and Xiao-Jing Gong. Strength prediction of a triaxially braided composite. *Composites Part A: Applied Science and Manufacturing*, 42(8):1000–1006, 2011. ISSN 1359-835X. doi: https://doi.org/10.1016/j.compositesa.2011.04.003. URL https://www.sciencedirect.com/science/article/pii/S1359835X11001096.

[27] Christopher R. Cater, Robert K. Goldberg, Xinran Xiao, and Lee W. Kohlman. *Improved Subcell Model for the Prediction of Braided Composite Response*. doi: 10.2514/6.2013-1618. URL https://arc.aiaa.org/doi/abs/10.2514/6.2013-1618.

[28] Christopher R. Cater, Xinran Xiao, Robert K. Goldberg, and Lee. W. Kohlman. Single ply and multi-ply braided composite response predictions using modified subcell approach. *Journal of Aerospace Engineering*, 28(5):04014117, 2015. doi: 10.1061/(ASCE)AS.1943-5525.0000445.

[29] Chris Sorini, Aditi Chattopadhyay, Robert K Goldberg, and Lee W Kohlman. Development of a subcell based modeling approach for modeling the architecturally dependent impact response of triaxially braided polymer matrix composites. Technical report, 2016.

[30] Christopher Cater, Robert K. Goldberg, Lee W. Kohlman, and Xinran Xiao. Experimental investigation and numerical analysis of the in-plane tensile behavior of a triaxially braided composite with subcell modeling approach. *Journal of Aerospace Engineering*, 31(5):04018052, 2018. doi: 10.1061/(ASCE)AS.1943-5525.0000872.

[31] A. García-Carpintero, M. Herráez, J. Xu, C. S. Lopes, and C. González. A multi material shell model for the mechanical analysis of triaxial braided composites. *Applied Composite Materials*, 24(6):1425–1445, 2017. doi: 10.1007/s10443-017-9593-9. URL https://doi.org/10.1007/s10443-017-9593-9.

[32] Stepan V. Lomov, Dmitry S. Ivanov, Ignaas Verpoest, Masaru Zako, Tetsusei Kurashiki, Hiroaki Nakai, and Satoru Hirosawa. Meso-fe modelling of textile composites: Road map, data flow and algorithms. *Composites Science and*

Technology, 67(9):1870–1891, 2007. ISSN 0266-3538. doi: https://doi.org/10.1016/j.compscitech.2006.10.017. URL https://www.sciencedirect.com/science/article/pii/S0266353806004027.

[33] Deepak Goyal. *Analysis of 2x2 braided composites*. PhD thesis, Texas A&M University, 2004.

[34] Deepak Goyal, Xiaodong Tang, John D. Whitcomb, and Ajit D. Kelkar. Effect of various parameters on effective engineering properties of 2 × 2 braided composites. *Mechanics of Advanced Materials and Structures*, 12(2):113–128, 2005. doi: 10.1080/15376490490493998.

[35] Shu Ching Quek, Anthony Waas, Khaled W. Shahwan, and Venkatesh Agaram. Compressive response and failure of braided textile composites: Part 2—computations. *International Journal of Non-Linear Mechanics*, 39(4):649–663, 2004. ISSN 0020-7462. doi: https://doi.org/10.1016/S0020-7462(03)00019-2.

[36] Xuetao Li. *Mesomechanical Model for Failure Study of Two Dimensional Triaxial Braided Composite Materials*. PhD thesis, University of Akron, University of Akron, 2010.

[37] Wieslaw K. Binienda and Xuetao Li. Mesomechanical model for numerical study of two-dimensional triaxially braided composite. *Journal of Engineering Mechanics*, 136(11):1366–1379, 2010. doi: 10.1061/(ASCE)EM.1943-7889.0000181.

[38] Xuetao Li, Wieslaw K. Binienda, and Robert K. Goldberg. Finite-element model for failure study of two-dimensional triaxially braided composite. *Journal of Aerospace Engineering*, 24(2):170–180, 2011. doi: 10.1061/(ASCE)AS.1943-5525.0000029.

[39] Lei Xu, Seong Jong Kim, Cheng-Huat Ong, and Sung Kyu Ha. Prediction of material properties of biaxial and triaxial braided textile composites. *Journal of Composite Materials*, 46(18):2255–2270, 2012. doi: 10.1177/0021998311431353.

[40] Haris Hameed Mian, Gang Wang, Rehan Jamshed, and Muhammad Aamir Raza. Fea of biaxial and triaxial braided composite for effective material property evaluation and effect of braiding angle on the dynamic behavior. In *Proceedings of 2013 10th International Bhurban Conference on Applied Sciences & Technology (IBCAST)*, pages 30–38, 2013. doi: 10.1109/IBCAST.2013.6512126.

[41] Mamadou Abdoul Mbacke. *Caractérisation et modélisation du comportement mécanique des composites tressés 3D : Application à la conception de réservoirs GNV*. Theses, Ecole Nationale Supérieure des Mines de Paris, December 2013. URL https://pastel.hal.science/pastel-00960667.

[42] Tobias Wehrkamp-Richter, Nelson V. De Carvalho, and Silvestre T. Pinho. A meso-scale simulation framework for predicting the mechanical response of triaxial braided composites. *Composites Part A: Applied Science and Manufacturing*, 107:489–506, 2018. ISSN 1359-835X. doi: https://doi.org/10.1016/j.compositesa.2018.01.028. URL https://www.sciencedirect.com/science/article/pii/S1359835X18300368.

[43] Tobias Wehrkamp-Richter, Nelson V. De Carvalho, and Silvestre T. Pinho. Predicting the non-linear mechanical response of triaxial braided composites. *Composites Part A: Applied Science and Manufacturing*, 114:117–135, 2018. ISSN 1359-835X. doi: https://doi.org/10.1016/j.compositesa.2018.08.011. URL https://www.sciencedirect.com/science/article/pii/S1359835X18303191.

[44] Ibrahim Goda and Jean-François Ganghoffer. Construction of first and second order grade anisotropic continuum media for 3d porous and textile composite structures. *Composite Structures*, 141:292–327, 2016. ISSN 0263-8223. doi: https://doi.org/10.1016/j.compstruct.2016.01.061. URL https://www.sciencedirect.com/science/article/pii/S026382231600074X.

[45] Chao Zhang, Wieslaw K. Binienda, Robert K. Goldberg, and Lee W. Kohlman. Meso-scale failure modeling of single layer triaxial braided composite using finite element method. *Composites Part A: Applied Science and Manufacturing*, 58:36–46, 2014. ISSN 1359-835X. doi: https://doi.org/10.1016/j.compositesa.2013.11.009. URL https://www.sciencedirect.com/science/article/pii/S1359835X13003187.

[46] Chao Zhang, Wieslaw K. Binienda, and Lee W. Kohlman. Analytical model and numerical analysis of the elastic behavior of triaxial braided composites. *Journal of Aerospace Engineering*, 27(3):473–483, 2014.

[47] A. García-Carpintero, Jian Xu, C.s Lopes, and Carlos González. A model for the generation of the geometrical meso-structure of a triaxially braided composites. 07 2015. doi: 10.13140/RG.2.1.2277.1602.

[48] Fredrik Stig and Stefan Hallström. A modelling framework for composites containing 3d reinforcement. *Composite Structures*, 94(9):2895–2901, 2012. ISSN 0263-8223. doi: https://doi.org/10.1016/j.compstruct.2012.03.009. URL `https://www.sciencedirect.com/science/article/pii/S0263822312001110`.

[49] Jonathan J Crookston, Sreedhar Kari, Nicholas A Warrior, I Arthur Jones, and Andrew C Long. 3d textile composite mechanical properties prediction using automated fea of the unit cell. *ICCM-16. Kyoto*, 2007.

[50] Badadjida Wintiba, Bernard Sonon, Karim Ehab Moustafa Kamel, and Thierry J. Massart. An automated procedure for the generation and conformal discretization of 3d woven composites rves. *Composite Structures*, 180:955–971, 2017. ISSN 0263-8223.

[51] Anqi Li, Karim Ehab Moustafa Kamel, Badadjida Wintiba, Joris J.C. Remmers, Marc G.D. Geers, and Thierry J. Massart. A level set-based procedure for the cohesive modeling of yarn–yarn contacts in woven composite rves. *Composite Structures*, 304:116356, 2023. ISSN 0263-8223.

[52] Jonathan Josiah Crookston. Prediction of elastic behaviour and initial failure of textile composites. 2004. URL `http://eprints.nottingham.ac.uk/10081/`.

[53] Johannes C Nitsche. *Lectures on minimal surfaces: vol. 1*. Cambridge university press, 1989.

[54] J. Monterde. Bézier surfaces of minimal area: The dirichlet approach. *Computer Aided Geometric Design*, 21(2):117–136, 2004. ISSN 0167-8396. doi: https://doi.org/10.1016/j.cagd.2003.07.009. URL `https://www.sciencedirect.com/science/article/pii/S0167839603001304`.

[55] Dominic Kafka and Daniel Wilke. Gradient-only line searches: An alternative to probabilistic line searches, 2020.

[56] Piervincenzo Giovanni Catera, Francesco Gagliardi, Domenico Mundo, Luigi De Napoli, Anna Matveeva, and Laszlo Farkas. Multi-scale modeling of triaxial braided composites for fe-based modal analysis of hybrid metal-composite gears. *Composite Structures*, 182:116–123, 2017. ISSN 0263-8223. doi: https://doi.org/10.1016/j.compstruct.2017.09.017. URL `https://www.sciencedirect.com/science/article/pii/S0263822317323644`.

[57] Van-Dung Nguyen, Ling Wu, and Ludovic Noels. Unified treatment of microscopic boundary conditions and efficient algorithms for estimating tangent operators of the homogenized behavior in the computational homogenization method. *Computational Mechanics*, 59(3):483–505, 2017.

[58] G. w. Du and P. Popper. Analysis of a circular braiding process for complex shapes. *The Journal of The Textile Institute*, 85(3):316–337, 1994. doi: 10.1080/00405009408631277. URL `https://doi.org/10.1080/00405009408631277`.

[59] J.H. van Ravenhorst and Remko Akkerman. Optimisation of the circular braiding process. In S.V. Lomov, editor, *TexComp-11 conference*, pages –, September 2013. 11th International Conference on Textile Composites Home 2013, TEXCOMP 2013 ; Conference date: 19-09-2013 Through 20-09-2013.

[60] José Rothkegel, Benjamin Renson, Michaël Bruyneel, and Ludovic Noels. Data and software of "development of a geometric modeling strategy for the generation of representative unit cells in 2d braids", 2024. URL `https://gitlab.onelab.info/cm3/cm3Braiding`.